UNIVERSITY OF CALIFORNIA

Los Angeles

Spin Dynamics for Radio Frequency Applications

A dissertation submitted in partial satisfaction of the

requirements for the degree Doctor of Philosophy

in Electrical and Computer Engineering

by

Kevin Quy Tanh Luong

2022

ABSTRACT OF THE DISSERTATION

Spin Dynamics for Radio

Frequency Applications

by

Kevin Quy Tanh Luong

Doctor of Philosophy in Electrical and Computer Engineering

University of California, Los Angeles, 2022

Professor Yuanxun Ethan Wang, Chair

Magnetic materials have distinct behaviors attributed to their underlying spin dynamics. At radio frequencies, these behaviors have long made magnetic insulators called ferrites essential in the design of nonreciprocal devices such as circulators or isolators. However, the capabilities offered by spin dynamics are far from being fully realized. This dissertation focuses on two features of spin dynamics in the context of their application to designing new radio frequency devices. The first part of the dissertation examines nonlinearities inherent in spin dynamics to propose a new type of magnetic field sensor called the radio frequency precession modulation (RPM) sensor. Existing sensor types are unable to achieve high sensitivities without being impractical in terms of size or power consumption which limits their potential usefulness. In contrast, RPM sensors simultaneously have high sensitivity, small size, and low power consumption. The theory of RPM sensors is developed and verified through simulation. A

prototype is constructed, and experimental characterizations are consistent with theoretical predictions. The prototype exhibits a sensitivity of 11.6 $pT/Hz^{1/2}$ with a volume of 0.056 mm^3 and a power consumption of -41 dBm which is already competitive with existing sensors. The second part of the dissertation examines the magnetoelastic coupling of spin dynamics to mechanical stress to analyze a new type of antenna called the mechanically driven magnetoelectric antenna. These antennas employ magnetoelectric multiferroic composites to achieve smaller sizes and higher efficiencies as compared to existing antennas. Given that the research on these antennas is still in its early stages, the approaches to modeling them have been largely deficient, particularly with regards to the magnetoelastic coupling component of their operation. For accurate modeling that provides guidance in design and operation, the physics of magnetoelastic coupling is considered. Material-dependent conditions that maximize the coupling are found, and symbolic expressions explicitly relating the coupling to operational parameters and material properties are derived. Comprehensive numerical evaluations of the expressions reveal characteristics of the coupling as well as the influence of the operational parameters and material properties. The results provide insight and serve as a foundation upon which more comprehensive models can be constructed.

The dissertation of Kevin Quy Tanh Luong is approved.

Clarice Aiello

Robert Candler

Benjamin Williams

Yuanxun Ethan Wang, Committee Chair

University of California, Los Angeles

2022

TABLE OF CONTENTS

LIST OF FIGURES

LIST OF TABLES

ACKNOWLEDGMENTS

This dissertation is based in part on material from the following publications:

K. Q. T. Luong, W. Gu, F. Fereidoony, L. Yeung, Z. Yao, and Y. E. Wang, "Radio Frequency Precession Modulation-Based Magnetic Field Sensors," *IEEE Access*, vol. 10, pp. 3756-3765, Jan. 2022, doi: 10.1109/ACCESS.2021.3140142.

K. Q. T. Luong and Y. E. Wang, "Analysis of Dynamic Magnetoelastic Coupling in Mechanically Driven Magnetoelectric Antennas," *Sensors*, vol. 22, no. 2, Jan. 2022, Art. no. 455, doi: 10.3390/S22020455.

Support for the research was provided by NSF Nanosystems Engineering Research Center for Translational Applications of Nanoscale Multiferroic Systems (TANMS) under NSF Cooperative Agreement EEC-1160504.

VITA

Education:

2019 M.S. in Electrical and Computer Engineering, University of California, Los Angeles.

2017 B.S. in Electrical and Computer Engineering, University of California, Los Angeles.

Publications:

K. Q. T. Luong, W. Gu, F. Fereidoony, L. Yeung, Z. Yao, and Y. E. Wang, "Radio Frequency Precession Modulation-Based Magnetic Field Sensors," *IEEE Access*, vol. 10, pp. 3756-3765, Jan. 2022, doi: 10.1109/ACCESS.2021.3140142.

K. Q. T. Luong and Y. E. Wang, "Analysis of Dynamic Magnetoelastic Coupling in Mechanically Driven Magnetoelectric Antennas," *Sensors*, vol. 22, no. 2, Jan. 2022, Art. no. 455, doi: 10.3390/S22020455.

W. Gu, K. Luong, Z. Yao, H. Cui, and Y. E. Wang, "Ferromagnetic Resonance-Enhanced Electrically Small Antennas," *IEEE Trans. on Antennas and Propag.*, vol. 69, no. 12, pp. 8304-8314, Dec. 2021, doi: 10.1109/TAP.2021.3090032.

Z. Yao, S. Tiwari, T. Lu, J. Rivera, K. Q. T. Luong, R. N. Candler, G. P. Carman, and Y. E. Wang, "Modeling of Multiple Dynamics in the Radiation of Bulk Acoustic Wave Antennas," *IEEE J. on Multiscale and Multiphys. Comput. Techn.*, vol. 5, pp. 5-18, 2020, doi: 10.1109/JMMCT.2019.2959596.

N. Platt, K. Luong, and J.T. Urban, “Downwind Chlorine Hazard Estimates For The 2015-2016 Jack Rabbit II Campaign,” *Int. J. of Environ. and Pollut.*, vol. 64, no. 1-3, pp. 145-160, 2018, doi: 10.1504/IJEP.2018.099154.

CHAPTER 1

INTRODUCTION

1.1 Motivation

The role of magnetic materials in radio frequency applications often differs significantly from their role in low frequency applications. At higher frequencies, the dynamical behaviors of the elementary particle spins from which the material magnetization originates significantly influences the material's response to a magnetic field. Starting in the 1950s, this fact was fervently researched to develop radio frequency devices with unique characteristics [1]. The anisotropic nature of the response was exploited to design nonreciprocal devices such as circulators and isolators. The bias-dependent nature of the response was exploited to design tunable devices such as variable phase shifters, tunable filters, and tunable resonators. Radio frequency devices based on magnetic materials are now in large part considered a mature technology. However, the surface has only been scratched with regards to application of magnetic materials at radio frequencies. Researchers have recently begun to investigate new applications that enable these materials to be used to their full potential. For example, the linear resonance properties of the materials have been used to improve the radiation efficiency of electrically small antennas [2]. In another example, the ability to couple magnetic fields to waves of the elementary particle spins has been used to design reconfigurable miniaturized radio frequency components [3].

The research in this dissertation is part of the effort to use magnetic materials to their full potential. It is presented in two parts, each of which investigates a new application. Following this chapter about the physics and properties of magnetics and magnetic materials relevant to the main research, the first part of the dissertation is dedicated to magnetic field sensing. Chapter 2 proposes a new approach to sense magnetic signals by utilizing nonlinearities inherent in spin dynamics.

Sensors based on this approach are theoretically characterized, and the concept is validated through simulation. A prototype sensor based on the approach is described in Chapter 3. The construction and experimental characterization of the sensor is detailed, and its performance is compared with both theoretical predictions and the performance of state of the art sensors. In this case, the new application is made possible by novel manipulation of magnetic materials; however, new applications are also made possible by novel magnetic materials themselves. A class of materials known as magnetoelastic multiferroics has emerged that enable electric field coupling to material magnetization and vice versa [4]. In the radio frequency domain, these materials have been proposed to design antennas with unique characteristics. The second part of this dissertation is dedicated to these antennas. Chapter 4 describes an analysis of the spin dynamics in magnetoelectric multiferroics from the perspective of guiding antenna design. Symbolic expressions are derived that quantify antenna performance and relate it to various operating conditions and material properties, and the expressions are numerically evaluated to draw insights. Finally, Chapter 5 concludes this dissertation by summarizing the collective research presented and commenting on some of the limitations of the research as well as on the future outlook of the two applications considered.

1.2 Magnetics

1.2.1 Units

Two systems of units tend dominate in the study and description of magnetics. The first is the cgs system and the second is the SI system. The cgs system tends to be used when magnetics is considered in isolation whereas the SI system tends to be used when magnetic and electric interactions are considered in conjunction [5]. The same approach will be adopted in this

dissertation where discussions concerning solely magnetics use the cgs unit system whereas discussions concerning electromagnetic interactions will use the SI unit system.

1.2.2 Magnetic Fields

Under the magnetostatic approximation, there are two sources from which magnetic fields originate. The first source is electric currents. The Biot-Savart law [6] describes the magnetic fields generated by an electric current and, in SI units, is given by

$$\boldsymbol{H}(\boldsymbol{r}) = \frac{I}{4\pi}\int \frac{d\boldsymbol{l} \times \widehat{\boldsymbol{R}}}{R^2}. \tag{1}$$

Here, $\boldsymbol{H}$ is the field in A/m at an observation point $\boldsymbol{r}$, I is the current in A, the integral is performed along and in the direction of the current, and $\boldsymbol{R}$ is a vector from the current to the observation point.

The second source is the magnetic moment associated with charged particles possessing finite angular momentum. This angular momentum $\boldsymbol{j}$ in general consists of an orbital component $\boldsymbol{l}$ which is due to motion of the particle, and a spin component $\boldsymbol{s}$ which is an intrinsic quantum mechanical quality. The magnetic moment $\boldsymbol{\mu}$ of the particle is proportional to its total angular momentum according to

$$\boldsymbol{\mu} = \gamma \boldsymbol{j}$$

where the constant of proportionality γ is known as the gyromagnetic ratio and has a value which in general depends on the relative contributions of $\boldsymbol{l}$ and $\boldsymbol{s}$ to $\boldsymbol{j}$ [7]. In cgs units, $\boldsymbol{\mu}$ is in emu, $\boldsymbol{j}$ is in erg·sec, and γ is in rad/sec·Oe.

1.3 Magnetic Materials

Practically, the magnetic moments associated with charged particles are significant when they are assembled to produce macroscopically magnetic materials. The magnetic behavior of a

magnetic material is described by a magnetization $\boldsymbol{M}$, defined under a continuum approximation as a magnetic moment volume density in emu/cm^3, supposing cgs units. For many magnetic materials, the magnetization is attributed to electrons and more specifically to the electron's spin given that its orbital angular momentum tends to be quenched [5]. In this case

$$\boldsymbol{M} = -\gamma \boldsymbol{S} \tag{2}$$

where $\boldsymbol{S}$ is the spin angular momentum volume density in erg·sec /cm^3, and $\gamma/2\pi$ is equal to 2.8 MHz/Oe.

In a magnetic field $\boldsymbol{H}$, the magnetization will tend to align with the field. This behavior is described with the Zeeman energy density W given by

$$W = -\boldsymbol{M} \cdot \boldsymbol{H} \tag{3}$$

where the units for W are erg/cm^3, and the units for $\boldsymbol{H}$ are Oe [7].

The magnetization of certain magnetic materials is attributed to permanent elementary moments that align at room temperature. These materials are said to be spontaneously magnetized, and they are practically important for their high susceptibilities and their ability to exist as permanent magnets. The alignment of neighboring moments, which may be parallel or antiparallel, is due to the exchange interaction [5] which is a quantum mechanical phenomenon. Spontaneously magnetized materials are considered exclusively in the remainder of this dissertation.

1.3.1 Properties

Spontaneously magnetized materials are characterized by several properties. The saturation magnetization M_s is one such property, and it describes a material's magnetization when neighboring moments are in alignment. In general, a spontaneously magnetized material will exist

in a state in which it is volumetrically divided into a number of domains, or local regions where the neighboring moments are in alignment [5]. The magnetization of each domain will be equal to the saturation magnetization; however, these magnetizations are not aligned with one another. As a result, the net magnetization of the material is less than its saturation magnetization. With the application of a sufficiently strong magnetic field, the domain magnetizations will align to minimize the Zeeman energy (3) in which case the net magnetization of the material will be equal to its saturation magnetization. In this state, the material is said to be saturated.

The demagnetization field $\boldsymbol{H}_d$ is a property that describes the magnetic field within a magnetic material that is produced by the elementary magnetic moments of the material. Supposing a saturated material, the moments on its surface will produce a field that is directed opposite to the magnetization, hence the name demagnetization field. This field is in general dependent on the material shape, size, and magnetic state $\boldsymbol{M}$. Characterization of the field is typically accomplished with what are called demagnetization factors N_x, N_y, and N_z where

$$H_{dx} = -N_x M_x$$

$$H_{dy} = -N_y M_y$$

$$H_{dz} = -N_z M_z.$$

(4)

The demagnetization factors are in general spatially dependent; however, for the special case of saturated magnetic materials with ellipsoidal geometries, they will be calculatable constants. For these materials, the factors will satisfy $N_x + N_y + N_z = 4\pi$ supposing cgs units, and the demagnetizing field will be uniform throughout the material [5].

Crystal anisotropy is a property that describes a magnetic material which has certain crystallographic directions along which its magnetization will preferentially align. This property

is a consequence of spin-orbit coupling, and the preferential directions are called easy directions. For a cubic crystal, the crystal anisotropy is associated with an energy density given by

$$W = K_0 + K_1(\alpha_1^2\alpha_2^2 + \alpha_2^2\alpha_3^2 + \alpha_1^2\alpha_3^2) + K_2(\alpha_1^2\alpha_2^2\alpha_3^2) + \cdots \quad (5)$$

where the α's are directional cosines of the magnetization with the crystal axes and the K's are material constants in erg/cm^3, supposing cgs units. For a hexagonal crystal, the crystal anisotropy is associated with an energy density given by

$$W = K_0 + K_1 \sin^2(\theta) + K_2 \sin^4(\theta) + \cdots \quad (6)$$

where θ is the angle between the magnetization and the c-axis of the crystal. For a polycrystal, the crystal anisotropy is a weighted average of the that of the grains making up the polycrystal. If the polycrystal does not have a crystallographic texture, or in other words its grains are randomly oriented, it will not exhibit a net crystal anisotropy [5].

Magnetostriction is a property that describes a magnetic material with dimensions that depend on the state of its magnetization. Like crystal anisotropy, magnetostriction is a consequence of spin-orbit coupling. It is characterized by what are called magnetostriction constants λ that represent measures of the fractional change in dimension of the material along a given direction as the material transitions from a demagnetized to a saturated state. The existence of magnetostriction necessarily entails the magneto-mechanical effect in which the magnetic state of a material is influenced by an applied stress. This effect is associated with an energy density called the magnetoelastic energy density [5]. For a cubic crystal with either <100> or <111> easy directions, this energy density is given by

$$W = -\frac{3\sigma\lambda_{100}}{2}\left(\alpha_1^2\beta_1^2 + \alpha_2^2\beta_2^2 + \alpha_3^2\beta_3^2 - \frac{1}{3}\right) - 3\sigma\lambda_{111}(\alpha_1\alpha_2\beta_1\beta_2 + \alpha_2\alpha_3\beta_2\beta_3 + \alpha_1\alpha_3\beta_1\beta_3) \quad (7)$$

where λ_{100} and λ_{111} correspond to the fractional change measured along a <100> and <111> direction of the crystal respectively, the β's are directional cosines of the applied stress with the crystal axes, and σ is the applied stress in dyne/cm^2. A positive value for σ represents a tensile stress whereas a negative value represents a compressive stress. For a hexagonal crystal with easy direction along the c-axis, the magnetoelastic energy density is given by

$$\begin{aligned} W = &-\sigma\lambda_A[(\alpha_1\beta_1 + \alpha_2\beta_2)^2 - (\alpha_1\beta_1 + \alpha_2\beta_2)\alpha_3\beta_3] \\ &- \sigma\lambda_B[(1-\alpha_3^2)(1-\beta_3^2) - (\alpha_1\beta_1 + \alpha_2\beta_2)^2] \\ &- \sigma\lambda_C[(1-\alpha_3^2)\beta_3^2 - (\alpha_1\beta_1 + \alpha_2\beta_2)\alpha_3\beta_3] - 4\sigma\lambda_D(\alpha_1\beta_1 + \alpha_2\beta_2)\alpha_3\beta_3. \end{aligned} \quad (8)$$

In this equation, the α's and β's are directional cosines with respect to a set of orthogonal axes defined such that the first axis is parallel to a basal axis of the crystal and the third axis is parallel to the c-axis of the crystal. For a polycrystal, the magnetoelastic energy density in general depends on the crystallographic texture. If the material does not have a crystallographic texture or if its grains exhibit isotropic magnetostriction, (7) can be applied with $\lambda_p \coloneqq \lambda_{100} = \lambda_{111}$ corresponding to any direction along which measurement and saturation are taken.

1.3.2 Dynamics

The previous properties of a spontaneously magnetized material characterize it and are useful in understanding both the equilibrium magnetic state of the material as well as the process involved as the material transitions from a demagnetized to magnetized state. The dynamics of a spontaneously magnetized material describe the response of its magnetization to time-varying stimuli. From (2) and (3), and introducing a phenomenological term to account for losses arising

from the coupling of electron spin dynamics to lattice vibrations [7], the spatial and temporal evolution of magnetization can be expressed as

$$\frac{\partial \boldsymbol{M}}{\partial t} = -\gamma(\boldsymbol{M} \times \boldsymbol{H}_e) + \frac{\alpha}{M_s}\left(\boldsymbol{M} \times \frac{\partial \boldsymbol{M}}{\partial t}\right) \quad (9)$$

known as the Landau-Lifshitz-Gilbert equation. Here, $\boldsymbol{H}_e$ is an effective magnetic field which accounts for true magnetic fields as well as the influence of material properties on magnetization dynamics. The losses are characterized by the unitless constant α, known as the Gilbert damping constant. It is often specified indirectly with a material parameter ΔH known as the linewidth and defined as

$$\Delta H = \frac{2\alpha\omega}{\gamma} \quad (10)$$

where ω is the angular frequency of operation and the units of ΔH are Oe.

1.3.3 Ferrites

When the neighboring moments of a spontaneously magnetized material both align in an antiparallel configuration and are unequal in magnitude, the material is classified as ferrimagnetic. Amongst ferrimagnetic materials, oxides known as ferrites have been of considerable interest in the realm of radio frequency applications due to their insulating nature, which enables their use at high frequencies while avoiding eddy current losses, combined with their moderate saturation magnetizations and low damping at high frequencies [8]. Ferrites have been used extensively for the design of devices such as circulators, phase shifters, and filters [9].

Amongst ferrites, yttrium iron garnet $Y_3Fe_5O_{12}$ (YIG) is overwhelmingly the material of choice for radio frequency applications. Its industrial significance is accompanied by a wide

availability and mature processing methods that can produce high quality thin films and single crystals [9]. YIG has a saturation magnetization $4\pi M_s$ of 1750 G and, in single crystal form, it can have linewidths as low as 0.2 Oe at 1 GHz [10].

1.3.4 Magnetoelectric Multiferroics

Magnetoelectric multiferroics are a relatively new class of materials which exhibit ferromagnetism as well as ferroelectricity, where the material exhibits a spontaneous electric polarization. Interest in these materials lies in the coupling between their magnetic and electric behaviors. This coupling enables a unique capability to control magnetism via electric fields or electric polarization via magnetic fields. Magnetoelectric multiferroic materials can be either single-phase or composite, in which distinct materials that may individually possess ferromagnetism or ferroelectricity are combined. Single phase materials possess a direct coupling between their electric and magnetic behaviors whereas composite materials achieve an indirect coupling that is mediated by strain [4]. Magnetoelectric multiferroics have been used in applications ranging from energy efficient memories to targeted drug delivery vehicles to photovoltaic devices [11].

CHAPTER 2

RF PRECESSION MODULATION

2.1 Motivation

2.1.1 Magnetic field sensors

Magnetic field sensors have been one of the cornerstone technologies responsible for the progress in research and development in many areas, from geophysics to biomedicine to communications [12]. To meet the demands of the diverse range of applications that employ magnetic field sensors, a number of different approaches to sensing have emerged. For example, super quantum interference device (SQUID) sensors operate based on the quantization of magnetic flux, optically pumped sensors operate based on atomic magneto-optic effects, induction sensors operate based on Faraday's law, and magnetic tunnel junction sensors operate based on polarization dependent electron tunneling [12].

Magnetic field sensors have characteristics that depend strongly on their approach to sensing. A defining characteristic is sensitivity, or the lowest field value a sensor can detect above the noise floor in a unit of output bandwidth [13]. Higher sensitivity corresponds to the ability to detect weaker fields and is especially appealing for modern applications where working with weak fields is the norm. Apart from sensitivity, size and power consumption are also important characteristics. Both influence the practicality of a given sensor and thus its suitability for a given application. Smaller and lower power sensors are of course more practical.

2.1.2 Sensor Types

State of the art magnetic field sensors tradeoff sensitivity with practicality. Revisiting the sensor types introduced earlier, SQUID sensors are widely recognized to be the most sensitive.

They can achieve sensitivities better than 1 $fT/Hz^{1/2}$; however, they require cryogenic cooling which leads to a system that is large and costly in terms of both construction and power consumption [14]. Optically pumped sensors can be competitive with SQUID sensors in sensitivity, but require optically pumped, heated atomic vapor cells which again contribute to a large and costly system that is complex to design and manufacture [12] [15]. In [16], an optically pumped sensor achieves sub-$pT/Hz^{1/2}$ sensitivities in the kHz to MHz frequency range but requires a sensor volume of 57 mm^3 and power consumption on the order of tens of watts. Inductive sensors boast zero power consumption while also being able to achieve sensitivities better than 1 $fT/Hz^{1/2}$; however, this generally requires the device to be prohibitively large or heavy [17]. In [18], an inductive sensor achieves sub-$fT/Hz^{1/2}$ sensitivity in the hundreds of Hz to hundreds of kHz frequency range but requires a sensor area of more than 24 m^2. Magnetic tunnel junctions can be made extremely small; however, they consume moderate amounts of power and achieve moderate sensitivities. In [19], a MgO based magnetic tunnel junction sensor was constructed with a sensor area of just 676 um^2 but it achieves a sensitivity of only 97 $pT/Hz^{1/2}$ at 10Hz and has a power consumption of around -7dBm.

2.1.3 Contribution

To address the lack of a practical, high sensitivity magnetic field sensor, a new type of sensor is proposed. This sensor uses a unique approach to sensing that exploits the nonlinearities inherent in magnetization dynamics to achieve parametric amplification at radio frequencies. The approach is called radio frequency precession modulation (RPM). Unlike fluxgate sensors which rely on nonlinearities in the magnetization process and the periodic transition of a material between saturated and unsaturated states [20], RPM sensors rely on nonlinearities in the magnetization dynamics of materials maintained in saturation. Consequently, RPM sensors are not subject to the

Barkhausen noise that limits fluxgate sensor sensitivity [20]. Unlike the sensors of [21] or [22] which also rely on nonlinearities in the magnetization dynamics of materials maintained in saturation, RPM sensors are based on parametric amplification. The sensor of [21] is based on magnetostatic wave bandgaps, and the sensor of [22] is based on resonance induced phase shifts.

The basic concept of the RPM approach to magnetic field sensing is presented followed by a discussion of considerations for the realization of RPM sensors. A rigorous analysis of the operation of RPM sensors is performed, and symbolic expressions are derived to characterize them. Lastly, simulations are used to verify the analysis. Some potential applications that would be suitable for RPM sensors would include underground and underwater communications [23], space plasma research [24], or low-cost magnetic resonance imaging [25]. The construction and measurement of a prototype sensor is detailed in Chapter 3.

2.2 Concept

2.2.1 Operation

Supposing a magnetic material biased to saturation with a field H_0, the LLG equation (9) indicates that the material magnetization $\boldsymbol{M}$ exhibits precession when perturbed from its alignment with the field and that the angular frequency of the precession ω is dependent upon the magnitude of the field. This is depicted in Figure 1 (a), where the axis of precession is seen to be parallel to H_0. Supposing now a magnetic signal $h_s(t)$ parallel to H_0 is impressed upon the material then the result is effectively a time-varying bias field $H_0 + h_s(t)$. Since ω is dependent on the magnitude of the bias field, this signal will modulate the frequency of precession. This is depicted in Figure 1 (b), where m_t denotes a component of the magnetization transverse to the bias field. By detecting the modulated frequency of precession, it is then possible to deduce, or sense, the impressed

magnetic signal. Given that the frequency of precession will lie in the radio frequency domain in practice, this concept is named RF precession modulation (RPM).

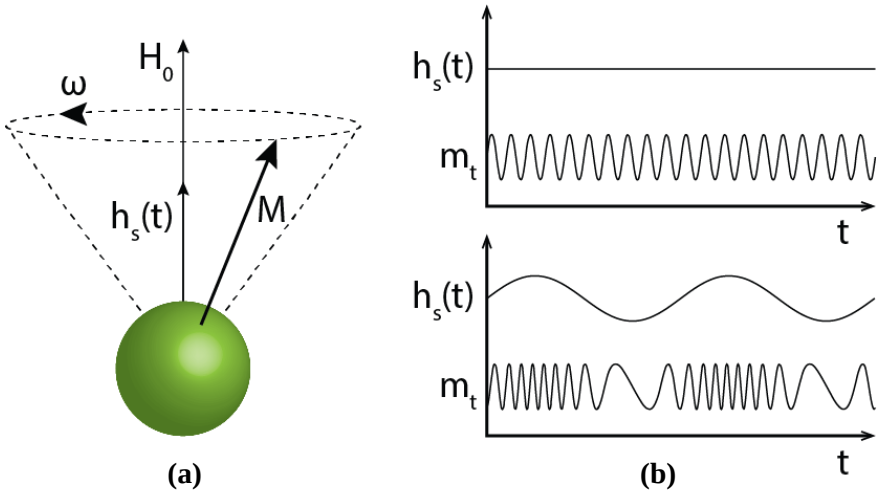

Figure 1. (a) Magnetization precession. (b) Time domain plot of the magnetic signal and the transverse component of magnetization showing field dependence of the precession frequency.

2.2.2 Sensor Design

Several design descisions must be taken into consideration when faced with the practicalities of realizing an RPM sensor. The first descision is with regards to the type of magnetic material to employ. With the frequencies of precession lying in the radio frequency domain, the most appropriate materials are ferrites. As discussed in section 1.3.3, ferrites are insulators with low damping at high frequencies. Both of these characteristics translate to lower loss in sensor operation which will be seen to contribute to better sensitivity performance. Of particular interest are thin-film ferrites given their potential for realizing extremely compact sensors.

The second decision is with regards to how precession is maintained. The damping of ferrites, despite how low it may be, is nevertheless finite. The LLG equation (9) indicates then that the magnetization undergoing precession will lose energy and eventually spiral back to into

re-alignment with the bias field. In order to maintain precession amidst the effects of finite damping, a pump field $h_p(t)$ is applied transverse to the bias field. This field is shown in Figure 2. It is useful to quantify the efficiency of the precession by associating with it a quality factor Q, defined as 2π times the average energy stored, divided by the energy lost per cycle [26].

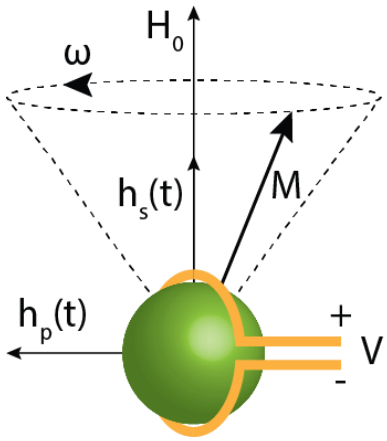

Figure 2. RF precession modulation (RPM) sensor.

The final descision is with regards to how the modulated frequency of precession is detected. As shown in Figure 2, an inductive approach is taken using a conductive loop. The loop is oriented to detect the component of magnetization transverse to the bias field m_t. Based on this decision, the energy referred to in the precession quality factor definition is the magnetic field energy of m_t. We can associate with this component of magnetization a time constant

$$\tau = 2Q/\omega. \tag{11}$$

defined as the time it takes for the component to decay by a factor $1/e$ supposing no pump field to maintain precession. Also based on this detection decision, the sensor can be modeled with the circuit of Figure 3, where R_0 is the resistance of the loop, L_0 is the inductance of the loop, I is a current source representing the transverse component of magnetization detected by the loop, V is the open circuit voltage induced by the component, and R_m, L_m, and C_m are in general dependent

on L_0 as well as the magnetic material biasing, saturation magnetization, and damping. Expressions for these last three components are provided in Appendix A.

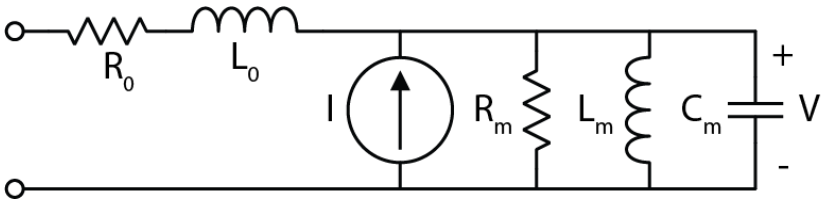

Figure 3. RPM sensor circuit model.

2.2.3 Inductive sensors

Inductive sensors are a good benchmark against which RPM sensors will be assessed. Not only are inductive sensors one of the most well-known sensor types, but their construction is very similar to that of RPM sensors in that it also involves conducting loops and, in many cases, ferrites. This similarity naturally facilitates comparison. The operation of inductive sensors is based on Faraday's law in which a magnetic signal directly induces a voltage in a conducting loop. The loop may have an air core or a ferrite core in which the linear relative permeability of an unbiased ferrite rod is used to magnify the magnetic flux coupled to the loop [17]. This in turn strengthens the voltage induced in the loop as compared to that of an air-core inductive sensor. A ferrite-core inductive sensor is shown in Figure 4.

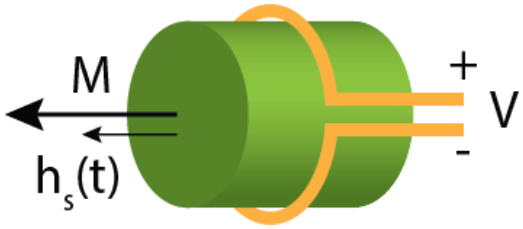

Figure 4. Ferrite-core inductive sensor.

2.3 Sensor Characteristics

An analysis of the characteristics of RPM sensors will follow two parallel developments. The first will consider a magnetic material in which demagnetization effects are negligible. Given

the interest in thin-film ferrites mentioned in section 2.2.2, the second development will consider a thin film magnetic body biased in-plane. In both the scenarios, a bias field of magnitude H_0 is applied. The angular frequency of precession set by this field will be referred to as the resonance frequency ω_0 of the material, and the pump field will be applied at this frequency according to

$$h_p(t) = H_p \cos(\omega_0 t).$$

(12)

The magnetic signal will be time-harmonic with an angular frequency ω_s and described by

$$h_s(t) = H_s \cos(\omega_s t + \phi_s)$$

(13)

where ϕ_s accounts for potential phase shifts of the signal. The conductive loop used to inductively detect the component of magnetization transverse to the bias field will have N turns and an area A equal to the cross-sectional area of the magnetic material. This loop is supposed to be unloaded for the analysis.

2.3.1 Dynamics of Operation

A rigorous account of the magnetization dynamics accompanying RPM sensor operation can be obtained with the LLG equation (9). In SI units, this equation is written as

$$\frac{\partial \boldsymbol{M}}{\partial t} = -\mu_0 \gamma (\boldsymbol{M} \times \boldsymbol{H}_e) + \frac{\alpha}{M_s}\left(\boldsymbol{M} \times \frac{\partial \boldsymbol{M}}{\partial t}\right)$$

(14)

where $\boldsymbol{M}$ and $\boldsymbol{H}_e$ have units of A/m, γ has units of C/kg, and μ_0 is the vacuum permeability with units of H/m. For the first scenario of a magnetic body where demagnetization effects are negligible, the resonance frequency can be found from (14) to be

$$\omega_0 = \mu_0 \gamma H_0$$

(15)

and the time constant of the transverse component of magnetization can be found to be [7]

$$\tau = 1/\alpha\omega.$$

(16)

From this result, (11) can be applied to find

$$Q = 1/2\alpha.$$

(17)

With the pump field and magnetic signal of (12) and (13) respectively, the transverse component of magnetization within a constant phase shift is given by

$$m_t = M_t \cos\left(\omega_0 t + \int_{t-\tau}^{t} \mu_0\gamma H_s \cos(\omega_s t + \phi_s)\, dt\right)$$

where M_t is the amplitude of this component. Under the assumption that $\omega_s\tau \ll 1$, the phase contribution from the magnetic signal can be simplified to write

$$m_t = M_t \cos(\omega_0 t + \mu_0\gamma H_s\tau \cos(\omega_s t + \phi_s)).$$

(18)

Further making the assumption that $\mu_0\gamma H_s\tau \ll 1$, (18) becomes

$$m_t = M_t \cos(\omega_0 t) - K_1 \sin(\omega_+ t + \phi_s) - K_1 \sin(\omega_- t - \phi_s)$$
$$K_1 = H_s M_t Q/H_0$$

(19)

where (11) and (15) are used and $\omega_\pm = (\omega_0 \pm \omega_s)$. This result indicates that the magnetic signal generates sidebands with angular frequencies $\omega_\pm$ in the magnetization precession. Detection of these sidebands allows for characterization of the signal.

Considering next the thin film magnetic body biased in-plane, the demagnetization field is significant, and it alters the magnetization dynamics significantly. In fact, the precession in this

scenario more closely resembles a pendulum oscillation [27], as shown in Figure 5. The resonance frequency can be found from (14) to be

$$\omega_0 = \mu_0 \gamma \sqrt{H_0(H_0 + M_s)}.$$

(20)

and the precession quality factor can be found to be [27]

$$Q = \frac{\sqrt{H_0(H_0 + M_s)}}{\alpha(2H_0 + M_s)}.$$

(21)

Applying (11) yields the associated time constant

$$\tau = \frac{2\sqrt{H_0(H_0 + M_s)}}{\alpha\omega(2H_0 + M_s)}.$$

(22)

With the pump field and magnetic signal of (12) and (13) respectively, the transverse component of magnetization within a constant phase shift is given by

$$m_t = M_t \cos\left(\omega_0 t + \int_{t-\tau}^{t} \frac{\mu_0 \gamma H_s(2H_0 + M_s)}{2\sqrt{H_0(H_0 + M_s)}} \cos(\omega_s t + \phi_s)\, dt\right)$$

(23)

under the assumption that $H_s \ll H_0$. Following an analogous procedure as in the scenario where demagnetization effects are neglected, (23) becomes

$$m_t = M_t \cos(\omega_0 t) - K_2 \sin(\omega_+ t + \phi_s) - K_2 \sin(\omega_- t - \phi_s)$$

$$K_2 = \frac{H_s(2H_0 + M_s)M_t Q}{2H_0(H_0 + M_s)}.$$

(24)

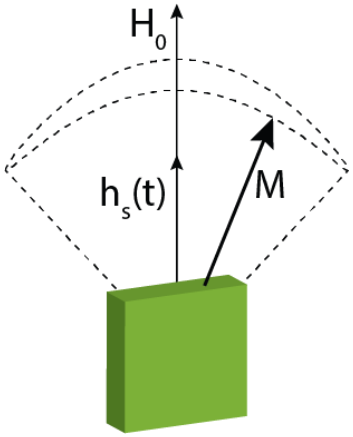

Figure 5. Magnetization precession of a thin film magnetic body biased in-plane.

Again, the result indicates that the magnetic signal generates sidebands with angular frequencies $\omega_{\pm}$ in the magnetization precession. From the dynamics described by (19) and (24) several characteristics of RPM sensors can be derived.

2.3.2 Sideband-to-Carrier Ratio

The results of section 2.3.1 indicate that the magnetization precession will have a carrier component with angular frequency equal to the material resonance frequency ω_0 as well as sideband components with angular frequencies $\omega_{\pm}$. This feature of RPM sensor operation can be characterized with a metric called the sideband-to-carrier ratio (SCR). As the name implies, it is a ratio of the magnitude of a sideband component to the carrier component. Considering the scenario of a magnetic material in which demagnetization effects are negligible, the detection of the carrier component of (19) will induce an open circuit rms voltage

$$V_0 = \frac{1}{\sqrt{2}}\mu_0 NAM_t\omega_0. \qquad (25)$$

The detection of a sideband component of (19) will induce an open circuit rms voltage

$$V_{RPM} = \frac{1}{\sqrt{2}}\mu_0^2\gamma NAH_sM_tQ = \frac{1}{2\alpha\sqrt{2}}\mu_0^2\gamma NAH_sM_t$$

(26)

where (15) and (17) are used, and it is assumed that $\omega_s \ll \omega_0$. The SCR is then found as the ratio of (26) to (25)

$$SCR = \frac{V_{RPM}}{V_0} = \frac{H_s}{H_0}Q = \frac{H_s}{\Delta H}$$

(27)

where the linewidth (10) in SI units is given by

$$\Delta H = \frac{2\alpha\omega}{\mu_0\gamma}.$$

(28)

Considering next the thin film magnetic body biased in-plane, an analogous procedure may be applied using (24). The detection of the carrier component will induce an open circuit rms voltage given by (25), and the detection of a sideband component will induce an open circuit rms voltage

$$V_{RPM} = \frac{\mu_0^2\gamma NAH_s(2H_0 + M_s)M_tQ}{2\sqrt{2H_0(H_0 + M_s)}} = \frac{1}{2\alpha\sqrt{2}}\mu_0^2\gamma NAH_sM_t$$

(29)

where (20) and (21) are used, and it is assumed that $\omega_s \ll \omega_0$. Then the ratio of (29) to (25) yields

$$SCR = \frac{H_s(2H_0 + M_s)Q}{2H_0(H_0 + M_s)} = \frac{H_s}{\Delta H}$$

(30)

where (28) is used. A comparison of (26) and (27) with (29) and (30) respectively reveals that, for RPM sensor operation at a given frequency, the voltage V_{RPM} as well as the SCR are independent of demagnetization effects.

2.3.3 Amplification

As discussed in section 2.2.3, RPM sensors will be compared against inductive sensors. One way in which this comparison is made is by characterizing RPM sensors based on the amplification they attain over inductive sensors. Employing the same loop with N turns and area A as an air-core inductive sensor, the magnetic signal will induce an open circuit rms voltage

$$V_i = \frac{1}{\sqrt{2}}\mu_0 NAH_s\omega_s. \tag{31}$$

The ratio of (26) to (31) is defined as the voltage amplification G_{RPM} of RPM sensors over air-core inductive sensors

$$G_{RPM} = \frac{V_{RPM}}{V_i} = \frac{M_t}{\Delta H}\frac{\omega_0}{\omega_s} \tag{32}$$

where (28) is used. This result holds for both the scenario where demagnetization effects are negligible and that where the magnetic material is a thin film biased in-plane. More generally, the voltage amplification for RPM sensor operation at a given frequency will be independent of demagnetization effects.

From (32), two distinct contributions to G_{RPM} may be identified. The first, corresponding to the product term $M_t/\Delta H$, is the coupling of a portion of the material magnetization to the detector. Greater coupling is achieved with greater pump power, higher saturation magnetization, or lower damping. The second contribution, corresponding to the product term ω_0/ω_s, is the

generation of sidebands by the magnetic signal. This contribution grows as the precession frequency increases or the magnetic signal frequency deceases. Both contributors clearly act to increase the electromotive force induced in the detector loop.

The amplification of (32) can also be viewed as the result of a method of parametric amplification. From this perspective, the RPM sensor is a resonant system where the bias field magnitude is seen from (15) and (20) to be the parameter upon which the resonance frequency is dependent. The pump field (12) harmonically drives the system at its resonance frequency while the magnetic signal (13) varies the parameter to produce amplification. This parametric amplification is made possible by the intrinsic nonlinear nature of magnetization dynamics and it is not contingent upon any external circuitry.

Values for G_{RPM} can be found supposing the magnetic material is YIG, described in section 1.3.3. Mirroring the measurements of Chapter 3, the material is biased for a resonance frequency of 1 GHz, in which case the linewidth can be as narrow as 0.2 Oe [10], and the magnetic signal is supposed to have a frequency of 10 kHz. The ideal maximum amplification, where a large pump field is applied such that $M_t \approx M_s$, can then be computed from (32) to be upwards of 178 dB. In practice however, the maximum amplification is limited by saturation effects caused by the generation of spin waves when the pump field is large [28].

2.3.4 Size

From (26) or (29), it is seen that G_{RPM} (32) also characterizes the size of RPM sensors as compared to inductive sensors. Specifically, the size of the RPM sensor A can be up to a factor G_{RPM} smaller than that of an air-core inductive sensor while still maintaining amplification. This assumes that the two sensors use conductive loops with the same number of turns. For the ideal

maximum amplification scenario described in section 2.3.3, the RPM sensor can be eight orders of magnitude smaller than an air-core inductive detector while still maintaining amplification.

2.3.5 Sensitivity and Power Consumption

The sensitivity of an RPM sensor is defined as the rms magnetic signal flux density

$$\delta B_s = \mu_0 H_s / \sqrt{2} \tag{33}$$

that yields a voltage V_{RPM} equal to the rms noise voltage in a unit of bandwidth V_n. The power consumption of an RPM sensor is the power required from the pump field to maintain precession. These characteristics are related using the results of section 2.3.1 in conjunction with the circuit model of Figure 3.

From the circuit model, two sources of noise can be identified. The first source, attributed to resistor R_0, is the thermal noise of the conductive loop. The second source, attributed to resistor R_m, is the damping noise of the magnetic material. In practice, it holds that $R_0 \ll R_m$, so the damping noise dominates and

$$V_n \approx \sqrt{4kTR_m} \tag{34}$$

where k is the Boltzmann constant in J/K, and T is the temperature in K.

Considering the scenario of a magnetic material in which demagnetization effects are negligible and using (27), (33), and (34), sensitivity can be expressed as

$$\delta B_{s,RPM} = \frac{\mu_0 H_0}{Q} \sqrt{\frac{2kTR_m}{V_0^2}} = \mu_0 \Delta H \sqrt{\frac{2kTR_m}{V_0^2}}. \tag{35}$$

The power consumption can be related to the sensitivity by defining power consumption based on the circuit model of Figure 3 to be $P_0 = V_0^2/R_m$. In this case, (35) becomes

$$\delta B_{s,RPM} = \frac{\mu_0 H_0}{Q}\sqrt{\frac{2kT}{P_0}} = \mu_0 \Delta H \sqrt{\frac{2kT}{P_0}}.$$

(36)

An analogous procedure yields, for a thin film magnetic material biased in-plane,

$$\delta B_{s,RPM} = \frac{2\mu_0 H_0 (H_0 + M_s)}{(2H_0 + M_s)Q}\sqrt{\frac{2kT}{P_0}} = \mu_0 \Delta H \sqrt{\frac{2kT}{P_0}}.$$

(37)

A comparison of (36) and (37) reveals that, for RPM sensor operation at a given frequency, the sensitivity is independent of demagnetization effects. These expressions specifically correspond to the inductive detection of a single sideband of precession; however (19) and (24) indicate that two sidebands exist. By detecting both sidebands and the using demodulation circuitry to coherently combine the induced voltages, sensitivity will improve and (36) and (37) will have an additional factor of $1/\sqrt{2}$.

Again, a comparison can be made against inductive sensors. Supposing now a ferrite-core inductive sensor that employs the same loop with N turns and area A, the sensitivity can be found to be

$$\delta B_{s,i} = \sqrt{\frac{4\mu_0 kT}{\mu_r v \omega_s Q_i}}$$

(38)

where μ_r is the relative permeability of the ferrite core, v is the volume of the loop, and Q_i is the quality factor of the loop. The derivation of (38) is provided in Appendix B. The ratio of (38) to (36) is the sensitivity improvement SI_{RPM} of RPM sensors attained over inductive sensors

$$SI_{RPM} = \frac{\delta B_{s,i}}{\delta B_{s,RPM}} = \frac{1}{\Delta H}\sqrt{\frac{2P_0}{\mu_r \mu_0 v \omega_s Q_i}}.$$

(39)

This improvement can be viewed in part as a result of the fact that the two contributions to the amplification G_{RPM}, discussed in section 2.3.3, manifest in the magnetization dynamics of the magnetic material prior to detection by the conductive loop. As a result, they do not amplify the thermal noise generated in the loop. In contrast, the air-core inductive sensor can achieve amplification only with additional circuitry that follows detection by the loop. This circuitry amplifies both the detected magnetic signal and the thermal noise generated in the loop. The ferrite-core inductive sensor achieves amplification prior to detection by the loop; however, this amplification is typically quite low with values around 50 being common [29]. Furthermore, due to their use of unbiased ferrites, ferrite-core inductive sensors are associated with additional magnetic losses that do not affect RPM sensors. These losses include hysteresis loss [30], domain wall resonance loss [31], and thermally agitated domain wall movement loss [32], all of which serve to increase noise and reduce sensitivity. These losses are not accounted for in (38) or (39).

Values for $\delta B_{s,RPM}$ can be found supposing, as in section 2.3.3, the magnetic material is YIG biased for a resonance frequency of 1 GHz and possessing a linewidth of 0.2 Oe. Then (36) indicates that sub-pT/Hz$^{1/2}$ sensitivity can be achieved with a pump power of just -24 dBm.

2.4 Simulation

The RPM concept was validated with micromagnetic simulations. These simulations numerically evaluate the LLG equation (9) for a magnetic material, and are called micromagnetic based on the resolutions typically considered which are large enough that the continuum approximation of magnetization holds yet small enough to faithfully represent the transition regions between magnetic domains [33]. The validation simulations were performed using the Object Oriented Micromagnetic Framework (OOMMF) [34], a program widely recognized as the standard for accurate micromagnetic solutions [35]. Within the program, a YIG thin film with dimensions 1 mm × 1 mm × 1 um and Gilbert damping constant α = 1e-3 was modeled. An in-plane bias field of 70 Oe was applied to set the resonance frequency at approximately 1 GHz. A time-harmonic pump field with amplitude 3.5e-2 Oe was applied at the resonance frequency to maintain precession. The amplitude of this field was chosen to be sufficiently small such that the assumptions employed in section 2.3.1 to derive the magnetization dynamics of RPM sensor operation are met. Lastly, a magnetic signal was applied with various amplitudes at a frequency of 50 kHz.

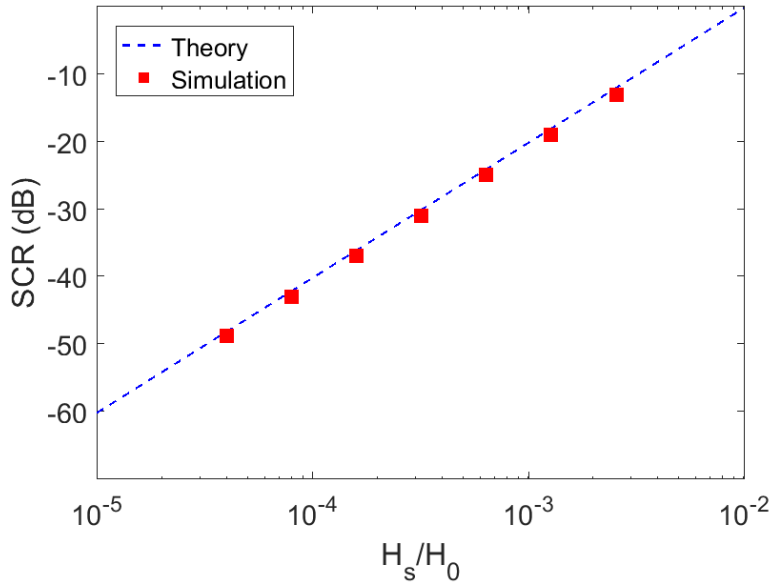

Figure 6. Sideband-to-carrier ratio results from micromagnetic simulations compared with RPM sensor theory.

A time-domain simulation with a total time evolution of 200 usec was performed for each of the magnetic signal amplitudes considered. The result of each of these simulations was transformed into the frequency domain using a fast Fourier transform algorithm, and the magnitudes of a sideband component and the carrier component of the magnetization precession were extracted. The ratio of these components, the SCR, was then found. The SCRs found through micromagnetic simulations are compared with those computed using (21) and (30) in Figure 6, which is a plot of the SCR in decibels as a function of the ratio of the magnetic signal amplitude to the bias field magnitude. Excellent agreement is exhibited between the simulation and the theory, which supports the validity of the RPM concept.

CHAPTER 3

RPM SENSOR PROTOTYPE

3.1 Hardware

The hardware involved in the construction and characterization of a prototype RPM sensor included a YIG epitaxial thin film on a GGG substrate [10] used for the magnetic material. The dimensions of the film were 3.76 mm × 5 mm × 3 um, corresponding to a sensor volume of 0.0564 mm^3, and the linewidth was found to be about 0.5 Oe at 1 GHz, inferior to its expected single crystal value. The details of how this linewidth was found are described in section 3.3.5. The film

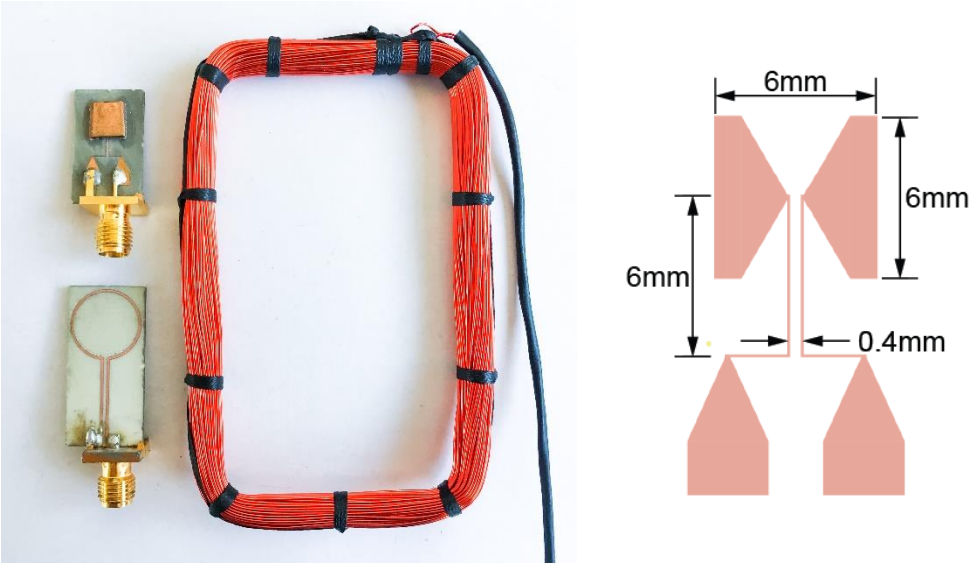

Figure 7. (a) Clockwise from top left: inductive detector, signal coil, pump loop.
(b) Inductive detector traces and dimensions.

was biased in-plane by placing it between two neodymium permanent magnets [36], and magnetization precession was maintained with a pump field produced from a single turn loop fabricated on a 0.813 mm thick Rogers RO4003C board with 35 um thick copper cladding [37]. This loop, shown in Figure 7 (a), had a trace width of 1 mm and a radius of 5.05 mm. The magnetic signal was produced from a 125 turn coil of 26 AWG copper wire. This coil is also shown in Figure

7 (a), and it had dimensions of 45 mm × 75 mm. Finally, the magnetization of the YIG thin film was detected inductively with a single turn loop constructed from a strip of copper soldered to traces that were fabricated on the same Rogers RO4003C board. This loop had dimensions of 6 mm × 6 mm × 1 mm and is shown in Figure 7 (a). The traces and their dimensions are shown in Figure 7 (b).

3.2 Signal-to-Carrier Ratio Measurement

3.2.1 Setup

Using the hardware described in section 3.1, SCR was measured for magnetic signals at various amplitudes and frequencies. A diagram of the measurement setup is shown in Figure 8 (a) and a photo is shown in Figure 9. The YIG film was placed within the inductive detector and the

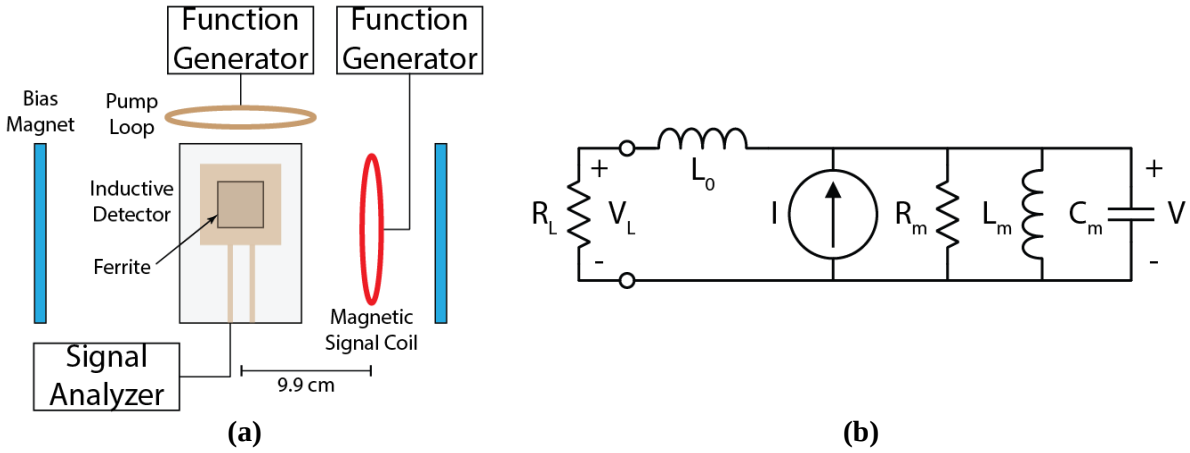

Figure 8. (a) Diagram of SCR measurement setup. (b) Circuit model of SCR measurement setup.

permanent magnets were positioned for a bias field of approximately 70 Oe corresponding to a resonance frequency of 1 GHz. The pump loop was positioned adjacent and coaxial to the detector and driven at the resonance frequency for a pump power of -50 dBm. This power was chosen to be sufficiently small such that the assumptions employed in section 2.3.1 to derive the magnetization dynamics of RPM sensor operation are met. The measurement of this power is

described in Appendix C. The magnetic signal coil was positioned 9.9 cm from the detector with its axis orthogonal to that of the detector and driven to produce signal fields of various amplitudes

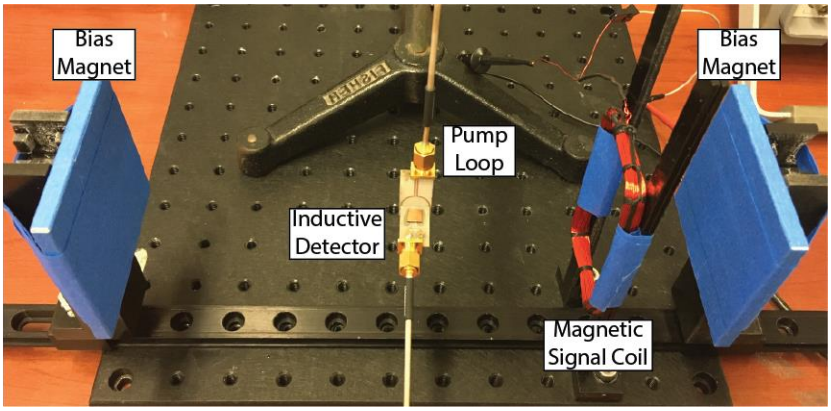

Figure 9. Photo of SCR measurement setup.

and frequencies. Specifically, both 1 and 2 V were applied to the coil at frequencies of 10, 30, and 50 kHz to produce the signal fields. The detector is connected directly to a signal analyzer to observe the spectrum of the induced voltage. The circuit model for the RPM sensor in the context of this setup is shown in Figure 8 (b), where the load resistance R_L is the 50 Ω input impedance of the signal analyzer and where the loop resistance is negligible. Details of the circuit model were originally discussed in section 2.2.2.

3.2.2 Results

The rms voltage induced in the detector by the magnetization precession manifests as a power dissipated in the signal analyzer. From the circuit model of Figure 8 (b), this power is V_L^2/R_L, where V_L is a linear function of the open circuit induced rms voltage V. Consequently, the measured SCR in dB can be found by taking a ratio of the power at a sideband frequency to that at the carrier frequency. This measured SCR is provided in the third column of Table 1. The spectrum of the power for a signal field frequency of 30 kHz is shown in Figure 10, where 1 and 2 V refers to the voltage applied to the signal coil. These results verify that RPM is achieved given that both the carrier and sideband components of magnetization precession are exhibited. It is seen

that doubling the voltage applied to the signal coil, which doubles the signal field according to (1), doubles the SCR as predicted by (30).

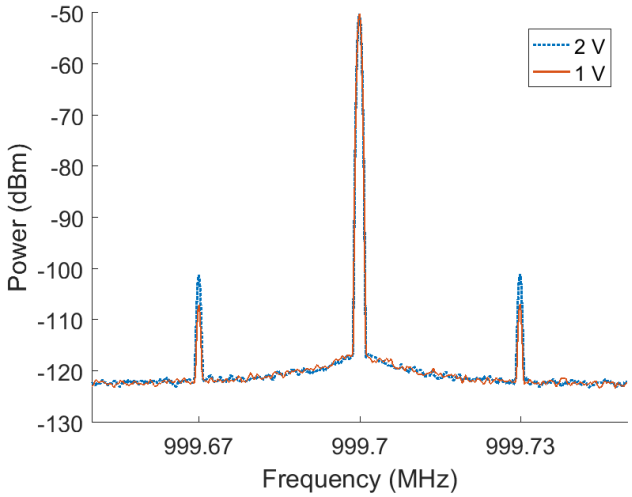

Figure 10. Power spectrum for a 30 kHz magnetic signal.

3.2.3 Comparison to theory

For a more complete comparison to the RPM sensor theory developed in section 2.3.2, (30) was used to directly compute the SCR. Specifically, the more general expression for SCR in terms of quality factor was employed given that the expression in terms of linewidth holds only in the ideal case of an open circuit detection, or in other words, when Q corresponds to that of an unloaded detector. The measurement setup involves a loaded detection and so Q corresponds to that of the loaded detector. The value of the loaded detector quality factor was found as the inverse of the fractional bandwidth of the loaded detector. This fractional bandwidth was measured using a vector network analyzer (VNA) and the value for Q was found to be about 136. Also required to compute (30), the bias field H_0 of 70 Oe was verified through gaussmeter measurements. Lastly, the signal field amplitude H_s was found by using a circuit model to determine the current through the signal coil then applying the Biot-Savart law (1). Details of the circuit model and the application of the Biot-Savart law are provided in Appendix D and E respectively. The computed

SCR values are provided in the last column of Table 1. All the values relevant to the computation are provided in Appendix F.

An examination of the last two columns of Table 1 shows that there is excellent agreement between the measured SCR values and those predicted from theory. This holds for all voltages as well as frequencies applied to the signal coil. The measured values are marginally less than those predicted from the theory in all cases. This may be attributed to the fact that the magnetic signal fields produced by the signal coil were not perfectly uniform, contributing to a lower system quality factor than if the fields were uniform.

Voltage (V)	Frequency (kHz)	Measured (dB)	Theoretical (dB)
1	10	-47.31	-46.93
	30	-56.82	-56.32
	50	-61.91	-61.28
2	10	-41.44	-40.91
	30	-50.96	-50.30
	50	-55.52	-55.26

Table 1. SCR measurements and comparison to theory.

3.3 Sensitivity Measurement

3.3.1 Setup

Using the hardware described in section 3.1, sensitivity was measured for magnetic signals at various frequencies. A diagram of the measurement setup is shown in Figure 11. The setup resembles that of the SCR measurement in many regards. The bias field remains at 70 Oe for a resonance frequency of 1 GHz. The pump loop was driven at the resonance frequency for a pump power of -41 dBm. The measurement of this power is described in Appendix C. The magnetic signal coil was positioned 7.7 cm from the detector and 10 mV was applied to it at frequencies of 10, 15, and 30 kHz to produce the signal fields.

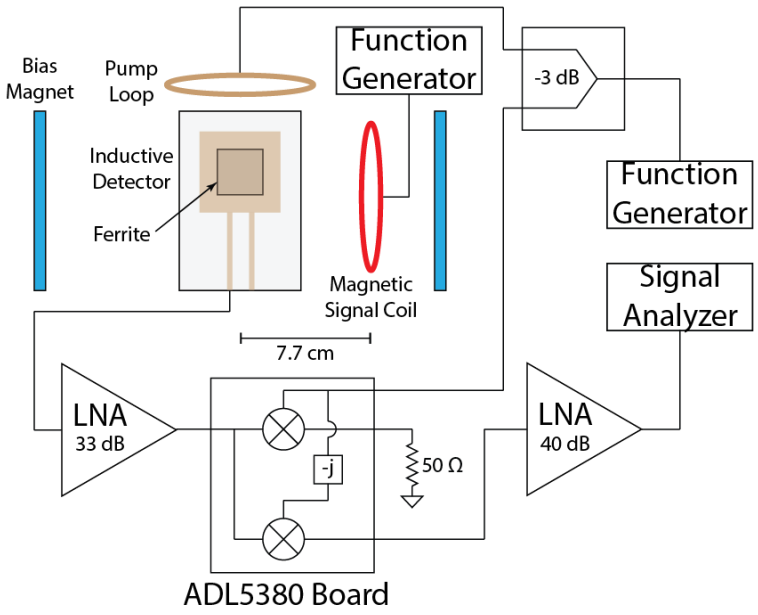

Figure 11. Diagram of sensitivity measurement setup.

Where this setup deviates significantly from that of the SCR measurement is with the detector connection. A direct connection of the detector to a signal analyzer was not suitable for a sensitivity measurement given that the noise of the system would be dominated by the phase noise of the pump field. To eliminate phase noise from the measurement, the voltage induced in the detector was coherently demodulated. This was accomplished by connecting the detector to the RF input port on an Analog Devices ADL5380 evaluation board [38] via a 33 dB low noise amplifier (LNA). The LO input port of the board was driven with the same function generator used to drive the pump loop, and the in-phase IF output port was connected to a signal analyzer via a 40 dB LNA to observe its spectrum. The quadrature phase IF output port was terminated with a matched load.

The circuit model for the RPM sensor in the context of this setup is shown in Figure 12, where the load resistance R_L is the 50 Ω input impedance of the 33 dB LNA, the loop resistance is negligible, and noise sources are explicitly shown. Here, the noise source producing rms voltage in a unit of bandwidth V_n represents the damping noise (34), and the noise source producing rms

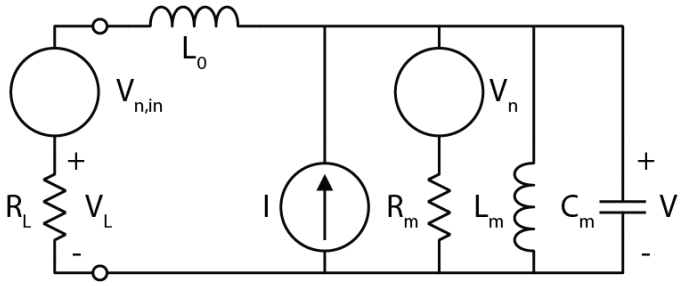

Figure 12. RPM sensor circuit model in sensitivity measurement setup.

voltage in a unit of bandwidth $V_{n,in}$ represents the total noise of the LNAs, the ADL5380 board, and the signal analyzer. By referring the noise of these electronics to the input of the 33 dB LNA in the circuit model, the measured sensitivity can be assessed based on the load voltage V_L.

3.3.2 Setup Implications

In the assessment of SCR, a comparison between the measured and theoretical values was made in section 3.2.3 using the more general form of the theoretical expression (30) in terms of quality factor. This form of the expression was required to account for the fact that the measurement setup involved a loaded detection. In the assessment of sensitivity, a comparison will likewise be made between the measured and theoretical values; however, the theoretical values will be computed as those corresponding to an unloaded detector. This choice was made to avoid misrepresenting the sensitivities attainable by RPM sensors due to a lack of low noise electronics available for the measurement setup. The theoretical sensitivity will then be computed using the expression

$$\delta B_{s,RPM} = \frac{2\mu_0 H_0 (H_0 + M_s)}{(2H_0 + M_s) Q_u} \sqrt{\frac{kT}{P_0}} \quad (40)$$

where Q_u is used to denote specifically the quality factor of the unloaded detector and where the use of demodulation circuitry in the measurement setup entails that (40) differ from (37) by a factor $1/\sqrt{2}$, as discussed in section 2.3.5.

The effect of a loaded detection in the measurement setup has two primary implications that must be in accounted for in order to compare the measured results with the theoretical ones computed using (40). The first is that the quality factor of the loaded detector Q_L will differ from that of the unloaded detector Q_u. The second is that the measured sensitivity $\delta B_{s,L}$ will be affected by noise contributions from both damping and measurement electronics. This is evident in the circuit model of Figure 12. In contrast, (40) was derived under the assumption that only damping noise is significant. An expression for the measured sensitivity can be obtained by first using Figure 12 to recognize that the rms load voltage V_L corresponding to the detection of magnetization precession at a sideband frequency has two components

$$V_L = V_{L,RPM} + V_{n,L}$$

$$V_{L,RPM} = \frac{R_L}{\sqrt{(R_L + R_m)^2 + \omega^2 L_0^2}} V_{RPM}$$

$$V_{n,L} = \frac{R_L}{\sqrt{(R_L + R_m)^2 + \omega^2 L_0^2}} \sqrt{V_n^2 + V_{n,in}^2}$$

(41)

where $V_{L,RPM}$ is the information bearing signal and $V_{n,L}$ is the noise. The measured sensitivity is the rms magnetic signal flux density that yields $V_{L,RPM}$ equal to $V_{n,L}$. Using (41) and (30) and accounting for the factor $1/\sqrt{2}$ arising from the use of demodulation circuitry, the measured sensitivity is

$$\delta B_{s,L} = \frac{2\mu_0 H_0 (H_0 + M_s)}{(2H_0 + M_s) Q_L} \sqrt{\frac{V_n^2 + V_{n,in}^2}{4V_0^2}}.$$

(42)

This can be related to (40) as

$$\delta B_{s,RPM} = \frac{Q_L}{Q_u} \sqrt{\frac{V_n^2}{V_n^2 + V_{n,in}^2}} \delta B_{s,L} = D_L \delta B_{s,L}$$

where D_L is called the load de-embedding factor. For the choice of measurement electronics used in the setup, it turns out that the total input-referred noise is dominated by the noise of the 33 dB LNA $V_{n,in} \approx V_{n,LNA}$, in which case the load de-embedding factor is given by

$$D_L \approx \frac{Q_L}{Q_u} \frac{V_n}{\sqrt{V_n^2 + V_{n,LNA}^2}} = \frac{Q_L}{Q_u} \left(1 + \frac{T_{LNA} R_L}{T_0 R_m}\right)^{-\frac{1}{2}}$$

(43)

and T_{LNA}, the equivalent noise temperature of the 33 dB LNA, is739 K [39].

3.3.3 Results

The voltage induced in the detector by the sideband components of magnetization precession is demodulated by the ADL5380 evaluation board to produce an IF output at the magnetic signal frequency. This output ultimately manifests as an rms voltage in the high-impedance signal analyzer. The spectrum of the output rms voltage per unit bandwidth for a signal field frequency of 30 kHz is shown in Figure 13. The measured sensitivity is determined by first finding the signal field amplitude H_s and signal-to-noise ratio (SNR) associated with each signal field frequency. As described in section 3.2.3, H_s was found by using a circuit model to determine the current through the signal coil then applying the Biot-Savart law (1). The SNR was found as the square of the ratio between the output rms voltage at the signal frequency to the average output

rms noise voltage per unit bandwidth. In Figure 13, the SNR was 33.4 dB. The signal field amplitude was then scaled by the inverse square root of the SNR to determine the amplitude that would yield an output rms voltage at the signal frequency equal to the average output rms noise voltage per unit bandwidth. The measured sensitivity is finally determined as the rms magnetic flux density (33) corresponding to this scaled field amplitude. The load de-embedding factor (43) is applied to enable comparison with the theoretical values that will be computed using (40), and the result is provided in the last column of Table 2. All the values relevant to the computation of this result are provided in Appendix G.

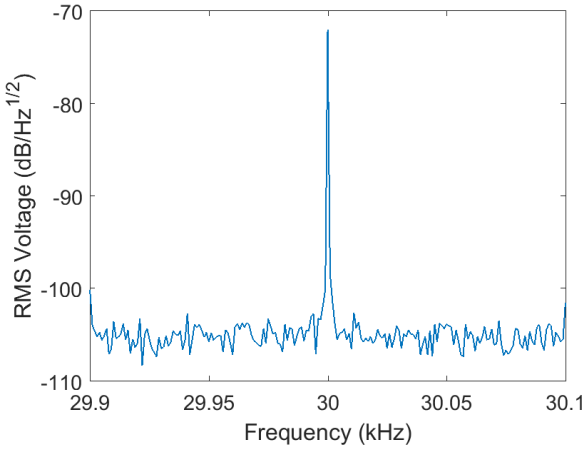

Figure 13. Voltage spectrum of demodulated IF output for a 30 kHz magnetic signal.

3.3.4 Comparison to theory

The measured sensitivity results are compared to the sensitivity computed theoretically using (40). For this computation, the bias field H_0 of 70 Oe was verified through gaussmeter measurements. The value of the unloaded detector quality factor Q_u was about 272—double that of the loaded detector quality factor found through the method discussed in section 3.2.3. This relation between the unloaded and loaded quality factors holds given that it was found from VNA measurements that the prototype RPM sensor is matched to 50 Ω at the resonance frequency. The

pump power P_0 of -41.0 dBm was determined based on VNA measurements as described in Appendix C. The theoretically computed sensitivity is provided in the third column of Table 2, and all the values relevant to the computation are provided in Appendix G. Also provided in this table is the theoretical sensitivity of the detector loop used as an air-core inductive sensor. These results were computed using (38) where the loop resistance R_0 is approximately 1 Ω. Lastly, the table provides results for the sensitivity improvement computed using (39).

Frequency (kHz)	Theory – Inductive Sensor ($pT/Hz^{1/2}$)	Theory – RPM Sensor ($pT/Hz^{1/2}$)	Theory – Sensitivity Improvement	Measurement – RPM Sensor ($pT/Hz^{1/2}$)
10	335.6	11.1	30.2	13.5
15	223.7	11.1	20.1	13.5
30	111.9	11.1	10.1	11.6

Table 2. Sensitivity results.

An examination of the third and last columns of Table 2 shows that the measured and theoretical sensitivities agree very well for all signal frequencies considered. Whereas the theory predicts that sensitivity is independent of the signal frequency, the measurements show that it worsens slightly as frequency drops. This may be attributed to the fact that lower frequencies correspond to higher system losses due to out-of-band operation of the ADL5380 evaluation board. There are several factors that contribute to the fact that the measured sensitivities as a whole are lower than the sensitivities computed theoretically. One factor, as mentioned in section 3.2.3. is the fact that the magnetic signal fields produced by the coil were not perfectly uniform, contributing to a lower loaded quality factor than if the fields were uniform. Another factor is the fact that the only significant source of noise in the theory is damping noise. In the measurement setup, thermal noise from the measurement electronics as well as phase noise from the pump field are also significant. To enable a comparison with theory, the thermal noise was accounted for with the de-embedding factor (43), and the phase noise was accounted for with coherent demodulation. However, phase noise was not completely eliminated in the measurement due to the existence of

a finite time delay difference t_d between the RF and LO ports of the ADL5380 board. This time delay difference results in what is merely a suppression of the phase noise by a factor $4\sin^2(\omega_s t_d/2)$ [40] and it allows phase noise to contribute to degrading the sensitivity.

An examination of the fourth column of Table 2 shows that the implemented RPM sensor exhibits at least an order of magnitude sensitivity improvement over the inductive sensor for all magnetic signal frequencies considered. Nevertheless, these values are not a good representative of the extent to which improvement is possible. The reason for this is because the cross-sectional area of the RPM sensor, corresponding to the cross-sectional area of the YIG, is less than 0.2% of that of the inductive sensor. A comparison between sensors with the same area would yield a much larger sensitivity improvement.

3.3.5 Comparison to other sensors

Comparing the RPM sensor prototype to ferrite inductive sensors in literature which operate at similar frequencies, the inductive sensor of [23] achieves a sensitivity three orders of magnitude better than that of the RPM sensor but requires a volume five orders of magnitude greater. Additionally, this inductive sensor is narrowband and achieves its sensitivity under matched conditions whereas the RPM sensor demonstrates operation to at least 30 kHz, with the upper limit extending far beyond that, with an almost flat sensitivity. The inductive sensor of [41] achieves a sensitivity two orders of magnitude better than that of the RPM sensor but does so within a much smaller bandwidth and requires a volume five orders of magnitude greater. Table 3 compares characteristics of the RPM sensor with those of other types of compact magnetic field sensors. Here again, the values are not necessarily a good representative of the extent to which RPM sensors can outperform other sensor types. From the unloaded detector quality factor and using (21) and (10), the YIG epitaxial thin film used by the prototype sensor is found to have a

linewidth at 1 GHz of about 0.5 Oe, much inferior to its expected single-crystal value of about 0.2 Oe [10]. With a higher quality material, the RPM sensor sensitivity could immediately be improved by a factor of two.

Type	Size (mm^3)	Power (dBm)	Frequency (Hz)	Sensitivity ($pT/Hz^{1/2}$)	Reference
Optically Pumped	57	44.9	30e3 – 1000e3	<1	[16]
Magnetic Tunnel Junction	6.0e-8	-6.8	10 – 5e5	97 – 2	[19]
Fluxgate	8.0	15.3	0.01 – 25	2.3e4	[42]
RPM – Theory	5.6e-2	-41.0	10e3 – 30e3	11.1	
RPM – Experiment	5.6e-2	-41.0	10e3 – 30e3	11.6 – 13.5	

Table 3. Comparison of compact sensors.

CHAPTER 4

ANALYSIS OF DYNAMIC MAGNETOELASTIC COUPLING

4.1 Motivation

4.1.1 Mechanically Driven Magnetoelastic Antennas

The magnetoelectric multiferroic materials described in section 1.3.4 have recently been explored for their potential in designing what are called mechanically driven magnetoelectric antennas [43]. These antennas employ magnetoelectric multiferroic composites composed of a piezoelectric phase and a magnetostrictive phase. Electromagnetic wave radiation is achieved by the antenna through application of an electric voltage stimulus to the piezoelectric phase, which

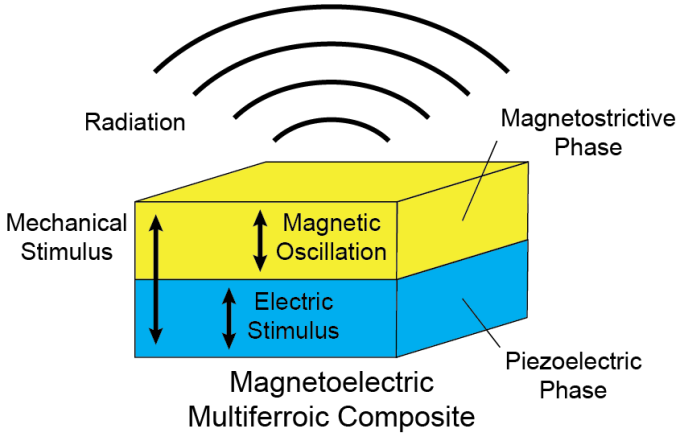

Figure 14. Mechanically driven magnetoelectric antenna.

transduces the stimulus into a mechanical one. The mechanical stimulus then couples to the magnetostrictive phase, inducing magnetic moment oscillation that generates radiation. This process is depicted in Figure 14. The radiated electric and magnetic fields for a dipole with magnetic moment m oscillating in free space with angular frequency ω are given by

$$\boldsymbol{E} = \frac{\mu_0 m\omega^2}{4\pi c}\left(\frac{\sin\theta}{r}\right)\cos[\omega(t - r/c)]\widehat{\boldsymbol{\phi}}$$

$$\boldsymbol{H} = -\frac{m\omega^2}{4\pi c^2}\left(\frac{\sin\theta}{r}\right)\cos[\omega(t - r/c)]\widehat{\boldsymbol{\theta}}.$$

(44)

Here, the dipole is at the origin of the coordinate system, oriented parallel to the z-axis, and the observation point is (r, θ, ϕ) in spherical coordinates. These equations are given in SI units with c being the speed of light in free space. Electromagnetic wave reception is achieved by the antenna in an analogous but reversed procedure.

Mechanically driven magnetoelectric antennas claim several advantages over conventional antennas that generate radiation with oscillating electric currents. One advantage is that the mechanically driven magnetoelectric antennas can be much smaller conventional antennas. The reason for this is because antenna dimensions are dictated by the size of the wavelength of operation. For conventional antennas, this wavelength is the electromagnetic wavelength [29] whereas for mechanically driven magnetoelectric antennas, this wavelength is the mechanical wavelength [43]. At a given frequency, mechanical wavelengths are many orders of magnitude smaller than electromagnetic wavelengths and so mechanically driven magnetoelectric antennas can have dimensions many orders of magnitude smaller than those of conventional antennas. Another advantage is that, because radiation is generated for mechanically driven magnetoelectric antennas through oscillating magnetic moments controlled by an electric voltage as opposed to oscillating electric currents, ohmic losses are eliminated to a large extent and antenna efficiency is improved [43]. The fact that the radiation is generated by oscillating magnetic moments also allows for operation of the antenna in the presence of a ground plane without the platform effect and the large storage of reactive energy that conventional antennas are subject to [44].

4.1.2 Modeling Approaches

While there has been progress in the realization of mechanically driven magnetoelectric antennas [43] [45], the approaches to modeling and understanding them have been largely inappropriate. Consequently, there are no concrete guidelines with regards to how the antennas should be designed or operated to maximize their radiative performance. Amongst the various types of coupling involved in the operation of mechanically driven magnetoelectric antennas, shown in Figure 15, magnetoelastic coupling in the magnetostrictive phase is identified to be in most need of scrutiny. This coupling has been shown to be crucial in determining antenna performance with larger amounts of coupling entailing stronger transduction between the mechanical stimuli and magnetic oscillations, leading to more efficient radiation [44].

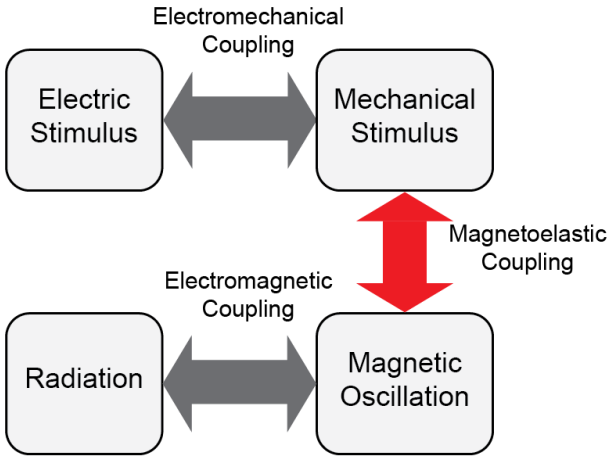

Figure 15. Types of coupling involved in mechanically driven magnetoelectric antenna operation.

Current approaches to modeling tend to neglect a consideration of magnetization dynamics in the treatment of magnetoelastic coupling. These approaches will describe magnetic behavior entirely through either linear [46] [47] or nonlinear [43] [48] frequency-independent constitutive equations. On the time scales associated with antenna operation at radio frequencies however, it is vital to account for the dynamics of magnetization. The behavior of the magnetic moments will be highly dependent on the time-varying nature of their excitation in ways that simply cannot be

described by frequency-independent constitutive equations. Current approaches also tend to neglect the significance of many of the operating conditions and magnetic material properties that influence magnetoelastic coupling. The use of constitutive equations accounts for these factors only implicitly, obscuring the nature of their influence. The significance of magnetization dynamics, operating conditions, and material properties on magnetoelastic coupling has been clearly demonstrated in studies involving magnetostrictive materials as well as magnetostrictive-piezoelectric multiferroic composites [49] [50]. While attempts have been made recently to incorporate magnetization dynamics into the modeling of mechanically driven magnetoelectric antennas [51], operating condition and material property effects are still largely hidden by the use of constitutive equations. Finally, current approaches to modeling tend to derive antenna performance from numerical simulations. These simulations provide little tangible insight to guide antenna design and operation choices.

4.1.3 Contribution

To address the issues plaguing current approaches to the modeling of magnetoelastic coupling in the magnetostrictive phase of mechanically driven magnetoelectric antennas, the LLG equation (9) is evaluated to obtain symbolic expressions quantifying the coupling. This equation enables the dynamics of magnetization to be fully considered. It also enables the explicit representation of the effects of antenna operating conditions and material properties through terms in the effective magnetic field $\boldsymbol{H}_e$. Symbolic expressions derived from the equation will reveal relationships between system parameters and magnetoelastic coupling that can guide antenna design and operation to maximize performance. This approach focuses solely on magnetoelastic coupling and so, in contrast with past approaches [43] [46] [48] [51], electrodynamics are not considered.

Mechanically driven magnetoelastic antennas will employ saturated magnetic materials to avoid the reductions in efficiency due to hysteresis loss [30] or domain wall resonance loss [31]. Operation involves perturbations of the material magnetization from its saturated state and so a linear analysis is suitable and employed throughout this work. This analysis supposes that both the magnetization and the effective magnetic field can be decomposed into a dominant static term and a time-varying perturbation, where the dominant terms are parallel to one another. This is described by

$$\boldsymbol{M} = M_s\hat{\boldsymbol{z}} + \boldsymbol{m}$$

$$\boldsymbol{H}_e = H_{ez}\hat{\boldsymbol{z}} + \boldsymbol{h}_e$$

(45)

with $|\boldsymbol{m}| \ll M_s$, $|\boldsymbol{h}_e| \ll H_{ez}$, and the dominant terms are chosen arbitrarily to align along the z-axis. The nature of antenna operation also entails that the analysis will ultimately assume the system to be time-harmonic. In this case, magnetoelastic coupling is quantified according to

$$\eta_i = m_i/\sigma$$

$$i \in \{x, y, z\}$$

(46)

where the η_i's are called the coupling coefficients and the m_i's are phasor components of the magnetization perturbation $\boldsymbol{m}$. To obtain symbolic expressions for the coupling coefficients, effective magnetic field terms are first derived to account for various antenna operating conditions and material properties of interest. The results are examined to extract conditions that will maximize magnetoelastic coupling. Symbolic expressions are then found in both a generalized form and forms tailored to specific scenarios by incorporating the effective magnetic field terms into the LLG equation. Finally, the expressions are numerically evaluated for a variety of materials and scenarios.

4.2 Effective Magnetic Field

Several operating conditions and material properties are of particular interest for mechanically driven magnetoelectric antennas. The operating conditions of interest are the stimulus frequency, applied magnetic biasing, and applied stress. Stimulus frequency will influence the response of the magnetic moments, magnetic biasing is important to ensure a saturated magnetic material with deterministic uniform magnetization, and stress is a fundamental mechanism upon which proper functionality of the antenna is contingent. The material properties of interest are the saturation magnetization, magnetic damping, crystal anisotropy, and demagnetization. These properties all play a significant role in affecting magnetization dynamics and the degree of magnetoelastic coupling that is achieved.

Amongst these operating conditions and material properties, stimulus frequency is implicitly accounted for with a time-harmonic analysis whereas saturation magnetization and magnetic damping are already inherently represented in the LLG equation. The other conditions and properties are accounted for with additive terms in the effective magnetic field. Magnetic biasing can be immediately accounted for as an actual field. Demagnetization can likewise be immediately accounted for based on the demagnetization field and demagnetization factors defined in (4). Applied stress and crystal anisotropy on the other hand, cannot be immediately accounted for. The influence of applied stress on magnetization is described with the magnetoelastic energy density (7), (8). The influence of crystal anisotropy on magnetization is described with the crystal anisotropy energy density (5), (6). Effective magnetic field terms can be derived from these energy densities according to

$$\boldsymbol{H}_e = -\frac{\partial W}{\partial \boldsymbol{M}}.$$

An overview of all the contributors to the effective magnetic field, along with expressions for their contribution is provided in Table 4.

Contributor	Effective Magnetic Field (Oe)
Applied Bias	$\boldsymbol{H}_0$
Applied Stress	
Cubic[1]	$\frac{3\sigma\lambda_{100}}{M_s^2}\left(u_x^2 M_x\hat{\boldsymbol{x}} + u_y^2 M_y\hat{\boldsymbol{y}} + u_z^2 M_z\hat{\boldsymbol{z}}\right) + \frac{3\sigma\lambda_{111}}{M_s^2}\left[\left(M_y u_y + M_z u_z\right)u_x\hat{\boldsymbol{x}} + \left(M_x u_x + M_z u_z\right)u_y\hat{\boldsymbol{y}} + \left(M_x u_x + M_y u_y\right)u_z\hat{\boldsymbol{z}}\right]$
	$\boldsymbol{H}_A + \boldsymbol{H}_B + \boldsymbol{H}_C + \boldsymbol{H}_D$
Hexagonal[2]	where $\boldsymbol{H}_A = \frac{\sigma\lambda_A}{M_s^2}\left(M_x u_x + M_y u_y\right)\left(2u_x\hat{\boldsymbol{x}} + 2u_y\hat{\boldsymbol{y}} - u_z\hat{\boldsymbol{z}}\right) - \frac{\sigma\lambda_A}{M_s^2}\left(M_z u_z\right)\left(u_x\hat{\boldsymbol{x}} + u_y\hat{\boldsymbol{y}}\right)$ $\boldsymbol{H}_B = -\frac{2\sigma\lambda_B}{M_s^2}\left[\left(M_x u_x + M_y u_y\right)u_x\hat{\boldsymbol{x}} + \left(M_x u_x + M_y u_y\right)u_y\hat{\boldsymbol{y}} + M_z(1-u_z^2)\hat{\boldsymbol{z}}\right]$ $\boldsymbol{H}_C = -\frac{\sigma\lambda_C}{M_s^2}u_z\left[M_z u_x\hat{\boldsymbol{x}} + M_z u_y\hat{\boldsymbol{y}} + \left(M_x u_x + M_y u_y + 2M_z u_z\right)\hat{\boldsymbol{z}}\right]$ $\boldsymbol{H}_D = \frac{4\sigma\lambda_D}{M_s^2}u_z\left[M_z u_x\hat{\boldsymbol{x}} + M_z u_y\hat{\boldsymbol{y}} + \left(M_x u_x + M_y u_y\right)\hat{\boldsymbol{z}}\right]$
Polycrystal	No general equation
Crystal Anisotropy[3]	
Cubic	$-\frac{2K_1}{M_s^2}\boldsymbol{M} + \frac{2K_1}{M_s^4}\left(M_x^3\hat{\boldsymbol{x}} + M_y^3\hat{\boldsymbol{y}} + M_z^3\hat{\boldsymbol{z}}\right)$
Hexagonal	$\frac{2K_1}{M_s^2}(\boldsymbol{M}\cdot\hat{\boldsymbol{z}})\hat{\boldsymbol{z}}$
Polycrystal	No general equation
Demagnetization	$(N_t - N_u)\left(\boldsymbol{M}\cdot\hat{\boldsymbol{d}}\right)\hat{\boldsymbol{d}}$

Table 4. Effective magnetic field contributions.

In this table, the applied bias contribution is a field $\boldsymbol{H}_0$. The applied stress, applied parallel to $\hat{\boldsymbol{u}}$, and crystal anisotropy contributions are sub-divided based on the crystal structure of the

[1] Valid for <100> or <111> easy directions.
[2] Valid when the easy direction is along the c-axis.
[3] Higher order terms are assumed to be negligible.

magnetic material. As discussed in section 1.3.1, there are no general equations for polycrystals, in which the magnetoelastic and crystal anisotropy energy densities depend on crystallographic texture. The expressions for cubic crystals assume the coordinate system axes to be aligned with <100> directions. The expressions for hexagonal crystals assume the z-axis to be aligned with the c-axis and one of either the x or y-axes to be aligned with a basal axis. The demagnetization contribution assumes that the magnetic material has a simple geometry such as a sphere, thin rod, or thin film. For these geometries, not only are the demagnetization coefficients approximately or exactly constant, but it will hold that two of the three coefficients are equal. In Table 4, N_t is the value of the equal coefficients, N_u is the value of the third coefficient, and $\hat{\boldsymbol{d}}$ is the direction corresponding to the third coefficient.

4.3 Applied Stress Optimization

The performance of mechanically driven magnetoelastic antennas is maximized by maximizing the magnetoelastic coupling. From (46), this will result a in larger magnetic moment perturbation which, from (44), will generate stronger radiated fields. Amongst the many potential parameters that can be optimized, the focus will be on applied stress. With magnetization given by (45), the optimal applied stress will be one that maximizes the effective field transverse to the dominant term. This maximizes the torque on the magnetization and consequently the degree to which the magnetization is perturbed.

From the equations of Table 4, the applied stress itself is seen to be associated with two parameters. The first is σ, the magnitude of which quantifies the amount of stress applied and the sign of which indicates whether the stress is tensile or compressive. The second parameter is $\hat{\boldsymbol{u}}$, which indicates the direction that the stress is applied. As discussed in section 4.1.3, a linear, time-harmonic analysis will be performed. Consequently, neither the magnitude nor the sign of σ will

affect the value of the coupling coefficients (46), and an optimal applied stress is tantamount to an optimal direction of application $\hat{\boldsymbol{u}}$.

4.3.1 Cubic Crystal <100>

For cubic crystals with <100> easy directions, it is reasonable to suppose that the dominant magnetization term will be aligned along one of these directions. With magnetization defined as in (45), the applied stress effective magnetic field expression provided in Table 4 can be employed directly since it assumes the coordinate system axes to be aligned with <100> directions. This expression can be written for the dominant magnetization term as

$$\boldsymbol{H}_e = \frac{3\sigma\lambda_{100}}{M_s} u_z^2 \hat{\boldsymbol{z}} + \frac{3\sigma\lambda_{111}}{M_s} \left[u_x u_z \hat{\boldsymbol{x}} + u_y u_z \hat{\boldsymbol{y}} \right].$$

The magnitude of the transverse component of the above is

$$|\boldsymbol{H}_{et}| = \left| \frac{3\sigma\lambda_{111}}{2M_s} \sin(2\theta) \right| \quad (47)$$

where θ is the angle between the applied stress direction and the direction of the dominant magnetization term. This result indicates that the optimal applied stress is directed at an angle 45° from the direction of the dominant magnetization term.

4.3.2 Cubic Crystal <111>

For cubic crystals with <111> easy directions, it is reasonable to suppose that the dominant magnetization term will be aligned along one of these directions. With magnetization defined as in (45), the applied stress effective magnetic field expression provided in Table 4 cannot be employed directly since it assumes the coordinate system axes to be aligned with <100> directions. A transformation between the coordinate system of (45), called the laboratory coordinate system, and the coordinate system of Table 4, called the crystal coordinate system, is needed. For a cubic

crystal with the [111] direction aligned with the z-axis of the laboratory coordinate system, the vector transformation from crystal to laboratory coordinate system used is

$$\boldsymbol{T} = \begin{bmatrix} -1/\sqrt{2} & 1/\sqrt{2} & 0 \\ -1/\sqrt{6} & -1/\sqrt{6} & 2/\sqrt{6} \\ 1/\sqrt{3} & 1/\sqrt{3} & 1/\sqrt{3} \end{bmatrix}$$

with the transpose $\boldsymbol{T}^{\mathrm{T}}$ being the inverse transformation from laboratory to crystal coordinate system. Hereon, the prime symbol will distinguish vectors and vector components of the crystal coordinate system from those of the laboratory coordinate system. Applying $\boldsymbol{T}^{\mathrm{T}}$ to the dominant term of (45), then the effective magnetic field in the crystal coordinate system is

$$\boldsymbol{H}_e = \frac{3\sigma\lambda_{100}}{M_s\sqrt{3}}\left(u'^2_x\hat{\boldsymbol{x}}' + u'^2_y\hat{\boldsymbol{y}}' + u'^2_z\hat{\boldsymbol{z}}'\right) + \frac{3\sigma\lambda_{111}}{M_s\sqrt{3}}\left[\left(u'_y + u'_z\right)u'_x\hat{\boldsymbol{x}}' + \left(u'_x + u'_z\right)u'_y\hat{\boldsymbol{y}}' + \left(u'_x + u'_y\right)u'_z\hat{\boldsymbol{z}}'\right].$$

The transformation $\boldsymbol{T}$ can be applied to transform the above to the laboratory coordinate system and again to express the result in terms of $\hat{\boldsymbol{u}}$ components as opposed to $\hat{\boldsymbol{u}}'$ components. The magnitude of the transverse component is then found to be

$$|\boldsymbol{H}_{et}| = \left|\frac{\sigma}{M_s\sqrt{2}}\right|\sqrt{\left(2A_1u_xu_y + A_2u_xu_z\right)^2 + \left(A_1u_x^2 - A_1u_y^2 + A_2u_yu_z\right)^2}$$

$$A_1 = \lambda_{111} - \lambda_{100}$$

$$A_2 = \sqrt{2}(2\lambda_{100} + \lambda_{111}).$$

(48)

If stress is applied in the xz-plane, (48) simplifies to

$$|\boldsymbol{H}_{et}| = \left|\frac{\sigma\sin(\theta)}{M_s\sqrt{2}}\right|\sqrt{A_1^2\sin^2(\theta) + A_2^2\cos^2(\theta)}$$

and if stress is applied in the yz-plane, (48) simplifies to

$$|\boldsymbol{H}_{et}| = \left|\frac{\sigma \sin(\theta)}{M_s\sqrt{2}}\left(A_1 \sin(\theta) - A_2 \cos(\theta)\right)\right|.$$

where θ is the angle between the applied stress direction and the direction of the dominant magnetization term. This result indicates that the optimal applied stress direction in general depends on the magnetostriction constants of the material. It will be characterized by not only θ, but also ϕ, where $\hat{\boldsymbol{u}} = \cos(\phi)\sin(\theta)\,\hat{\boldsymbol{x}} + \sin(\phi)\sin(\theta)\,\hat{\boldsymbol{y}} + \cos(\theta)\,\hat{\boldsymbol{z}}$. It will be shown in section 4.5.2 that, for a given ϕ, the optimal θ will be approximately 45°, 90°, or 135° depending on the specific magnetic material.

4.3.3 Hexagonal Crystal

For hexagonal crystals with easy direction along the c-axis, it is reasonable to suppose that the dominant magnetization term will be aligned along that direction. With magnetization defined as in (45), the applied stress effective magnetic field expression provided in Table 4 can be employed directly since it assumes the coordinate system z-axis to be aligned with crystal c-axis. This expression can be written for the dominant magnetization term as

$$\boldsymbol{H}_e = -\frac{\sigma(\lambda_A + \lambda_C - 4\lambda_D)}{M_s} u_z\left(u_x\hat{\boldsymbol{x}} + u_y\hat{\boldsymbol{y}}\right) + \frac{2\sigma}{M_s}(-\lambda_B + \lambda_B u_z^2 - \lambda_C u_z^2)\hat{\boldsymbol{z}}$$

The magnitude of the transverse component of the above is

$$|\boldsymbol{H}_{et}| = \left|\frac{\sigma(\lambda_A + \lambda_C - 4\lambda_D)}{2M_s}\sin(2\theta)\right| \qquad (49)$$

where θ is the angle between the applied stress direction and the direction of the dominant magnetization term. This result, similar to that of section 4.3.1, indicates that the optimal applied stress is directed at an angle 45° from the direction of the dominant magnetization term.

4.3.4 Polycrystal

For polycrystals, the lack of a general equation describing the effective magnetic field contribution of applied stress implies the lack of a general equation for the optimal applied stress. Nevertheless, under the condition that the material does not have a crystallographic texture or if its grains exhibit isotropic magnetostriction, either (47) or (48) apply with $\lambda_p \coloneqq \lambda_{100} = \lambda_{111}$. The optimal applied stress is then directed at an angle 45° from the direction of the dominant magnetization term. This result is consistent with experimental demonstrations [49].

4.4 Magnetoelastic Coupling

4.4.1 Linearization

Symbolic expressions for the magnetoelastic coupling coefficients (46) are derived employing a linear, time-harmonic analysis. The LLG equation (9) is linearized using (45) and neglecting higher order powers of the perturbations. For an $e^{j\omega t}$ time-harmonic system, the linearized phasor form of (9) is then given by

$$\frac{1}{\gamma M_s}\begin{bmatrix} \gamma H_{ez} + j\omega\alpha & -j\omega & 0 \\ j\omega & \gamma H_{ez} + j\omega\alpha & 0 \\ 0 & 0 & 1 \end{bmatrix}\begin{bmatrix} m_x \\ m_y \\ m_z \end{bmatrix} = \begin{bmatrix} h_{ex} \\ h_{ey} \\ 0 \end{bmatrix}. \tag{50}$$

where H_{ez} is the constant dominant effective magnetic field term, m_x, m_y, m_z are phasors of the components of $\boldsymbol{m}$, and h_{ex}, h_{ey} are phasors of the components of $\boldsymbol{h}_e$.

The effective magnetic field contributions of Table 4 are also linearized by using (45) and neglecting higher order powers of the perturbations. Again, for an $e^{j\omega t}$ time-harmonic system, the results for H_{ez}, h_{ex}, and h_{ey} under several assumptions are provided in Table 5. These assumptions, made based on scenarios of interest, include the dominant magnetization term being directed along the applied bias field $\boldsymbol{H}_0 = H_0\hat{\boldsymbol{z}}$ and the applied stress being optimally directed. For

cubic crystals with the dominant magnetization term aligned with a <100> direction or hexagonal crystals with the dominant magnetization term aligned along the c-axis, the optimal direction of applied stress is known from (47) and (49) respectively. For cubic crystals with the dominant magnetization term aligned with a <111> direction, the optimal direction is material dependent so instead some sample directions were chosen. The applied stress effective magnetic field contributions are labeled in Table 5 by the crystal structure followed by the dominant magnetization term direction followed by the applied stress direction in the form (θ, ϕ), where again $\hat{\boldsymbol{u}} = \cos(\phi)\sin(\theta)\,\hat{\boldsymbol{x}} + \sin(\phi)\sin(\theta)\,\hat{\boldsymbol{y}} + \cos(\theta)\,\hat{\boldsymbol{z}}$. The crystal anisotropy effective magnetic field contributions are similarly labeled by the crystal structure followed by the dominant magnetization term direction.

Contributor	h_{ex}	h_{ey}	H_{ez}
Applied Bias	0	0	H_0
Applied Stress			
Cubic [100] (45º, ϕ)	$\frac{3\sigma\lambda_{111}}{2M_s}\cos\phi$	$\frac{3\sigma\lambda_{111}}{2M_s}\sin\phi$	0
Cubic [111] (45º, -45º)	$\frac{3\sigma\lambda_{100}}{2M_s\sqrt{2}}$	$-\frac{\sigma(2\lambda_{100}+\lambda_{111})}{2M_s\sqrt{2}}$	0
Cubic [111] (90º, 0º)	0	$-\frac{\sigma(\lambda_{100}+\lambda_{111})}{M_s\sqrt{2}}$	0
Hexagonal [0001] (45º, ϕ)	$(-\lambda_A-\lambda_C+4\lambda_D)\frac{\sigma}{2M_s}\cos\phi$	$(-\lambda_A-\lambda_C+4\lambda_D)\frac{\sigma}{2M_s}\sin\phi$	0
Polycrystal	No general equation		
Crystal anisotropy			
Cubic[4] [100]	$-\frac{2K_1}{M_s^2}m_x$	$-\frac{2K_1}{M_s^2}m_y$	0
Cubic [111]	0	0	$-\frac{4K_1}{3M_s}$
Hexagonal [0001]	0	0	$\frac{2K_1}{M_s}$
Polycrystal	No general equation		

Demagnetization[4]	$(N_t - N_u)\big(m_x d_x + m_y d_y\big)d_x$	$(N_t - N_u)\big(m_x d_x + m_y d_y\big)d_y$	$(N_t - N_u)M_s d_z^2$

Table 5. Linearized effective magnetic field contributions.

4.4.2 General Solution

Incorporating the linearized effective magnetic field contributions of Table 5, the linearized LLG equation (50) will have the general form

$$\begin{bmatrix} B_1 & -j\omega & 0 \\ j\omega & B_2 & 0 \\ 0 & 0 & 1 \end{bmatrix} \begin{bmatrix} m_x \\ m_y \\ m_z \end{bmatrix} = \gamma M_s \sigma \begin{bmatrix} C_1 \\ C_2 \\ 0 \end{bmatrix}$$

$$B_1 = \gamma H_{ez} - \gamma M_s \, h_{exo}/m_x + j\omega\alpha$$

$$B_2 = \gamma H_{ez} - \gamma M_s \, h_{eyo}/m_y + j\omega\alpha$$

$$C_1 = h_{exs}/\sigma$$

$$C_2 = h_{eys}/\sigma$$

where the phasor components h_{ex}, h_{ey} are decomposed into contributions from applied stress h_{exs}, h_{eys} and contributions from all other material properties and operating conditions h_{exo}, h_{eyo}. General expressions for the magnetoelastic coupling coefficients can then be found from the equation above to be

$$\eta_x = \gamma M_s \left(\frac{B_2 C_1 + j\omega C_2}{\omega_r^2 - \omega^2}\right)$$

$$\eta_y = \gamma M_s \left(\frac{B_1 C_2 - j\omega C_1}{\omega_r^2 - \omega^2}\right)$$

$$\omega_r = \sqrt{B_1 B_2}$$

(51)

[4] Under the magnetostatic limit. The general case requires a consideration of electrodynamics.

where η_z is zero under the conditions of the linear analysis. For more utility and insight, these expressions are tailored to specific scenarios.

4.4.3 Specific Scenarios

Suppose the applied bias dominates in the sense that all other contributors to the effective magnetic field, apart from the applied stress, can be neglected. This may be the case for example with a polycrystal having no crystallographic texture and an approximately spherical shape, or simply with a material for which $\boldsymbol{H}_0$ is sufficiently large. In this case, (51) becomes

$$\eta_x = \gamma M_s \left(\frac{\omega_r C_1 + j\omega C_2}{\omega_r^2 - \omega^2} \right)$$

$$\eta_y = \gamma M_s \left(\frac{\omega_r C_2 - j\omega C_1}{\omega_r^2 - \omega^2} \right)$$

$$\omega_r = \gamma H_0 + j\omega\alpha$$

(52)

where C_1 and C_2 depend on the applied stress contribution to the effective magnetic field. These constants will change with crystal type, crystal orientation with respect to the dominant magnetization term, and direction of applied stress.

Suppose now that crystal anisotropy also contributes significantly to the effective magnetic field. For a cubic crystal then the coefficient expressions of (52) hold, but with

$$\omega_r = \gamma H_0 + \gamma \frac{2K_1}{M_s} + j\omega\alpha$$

(53)

in the case where the dominant magnetization term is directed along the [100] direction, or

$$\omega_r = \gamma H_0 - \gamma \frac{4K_1}{3M_s} + j\omega\alpha$$

in the case where the dominant magnetization term is directed along the [111] direction. For a hexagonal crystal then the coefficient expressions of (52) hold with ω_r defined as in (53) in the case where the dominant magnetization term is directed along the c-axis. Here, K_1 would be the anisotropy constant associated with hexagonal anisotropy. These results indicate that the effect of crystal anisotropy is equivalent to that of a change in the applied bias field strength.

Suppose lastly that, in addition to the applied bias, demagnetization also contributes significantly to the effective magnetic field. Letting θ_d be the angle between $\hat{\boldsymbol{d}}$, defined as in Table 4, and the dominant magnetization term, then the two cases of θ_d equal to 0° and 90° are considered. With θ_d equal to 0°, then the coefficient expressions of (52) hold, but with

$$\omega_r = \gamma H_0 + \gamma(N_t - N_u)M_s + j\omega\alpha.$$

Akin to crystal anisotropy, demagnetization in this case has an effect that is equivalent to that of a change in the applied bias field strength. With θ_d equal to 90°, $\hat{\boldsymbol{d}}$ is chosen specifically to be directed along the x-axis. No loss in generality is incurred with this choice given that a coordinate transformation can always be made to satisfy it. The coupling coefficients are then found to be described by (51) with

$$B_1 = B_2 + \gamma(N_u - N_t)M_s$$
$$B_2 = \gamma H_0 + j\omega\alpha.$$

(54)

4.5 Numerical Evaluation

The general expressions for the magnetoelastic coupling coefficients (51) are numerically evaluated for various types of materials to gain further insights regarding the nature of magnetoelastic coupling and the effects of the operating conditions and material properties of interest.

4.5.1 Cubic crystal <100>

A magnetic material with a cubic crystalline structure and <100> easy directions is iron Fe. Some relevant characteristics of iron are provided in Appendix H. The general magnetoelastic coupling coefficients are computed using (51) and plotted as a function of the stimulus frequency in Figure 16 and Figure 17.

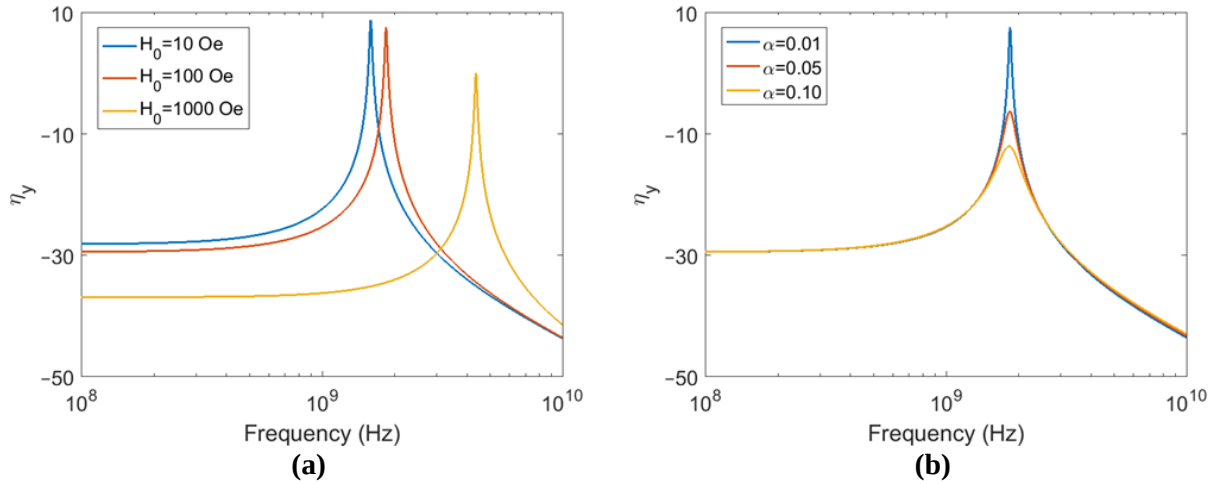

Figure 16. (a) Varying bias field. (b) Varying damping constant.

The effect of the applied bias is shown in Figure 16 (a), which is a plot of the magnitude of η_y for several bias field magnitudes. This plot has α set to 0.01 and optimal stress applied at an angle ϕ of 45° in the xy-plane, resulting in equal magnitudes for η_x and η_y. From the results, resonance behavior is exhibited, and the magnetoelastic coupling is seen to reach a peak value at some resonance frequency. Stronger biasing fields are shown to raise the resonance frequency while reducing the amount of coupling both at and below resonance.

The effect of damping is shown in Figure 16 (b), which is a plot of the magnitude of η_y for several damping constant values. This plot has the bias field set to 100 Oe and, again, optimal stress applied at an angle ϕ of 45° in the xy-plane such that the magnitudes for η_x and η_y are equal. From the results, larger damping is shown to lower the amount of coupling achieved at resonance, while having minimal effect on the amount of coupling achieved off-resonance.

The effect of demagnetization is shown in Figure 17. In Figure 17 (a), the magnitudes of both η_x and η_y are plotted for a magnetic material with a thin film geometry such that $N_t \approx 0$ and $N_u \approx 4\pi$. This plot has in-plane biasing with $\hat{\boldsymbol{d}} = \hat{\boldsymbol{x}}$, α set to 0.01, the bias field set to 100 Oe, and optimal stress applied at an angle ϕ of 45° in the xy-plane. From the results, demagnetization is shown to cause the magnetoelastic coupling to exhibit anisotropy with respect to the angle of stress application in the xy-plane. In particular, the amount of coupling to the in-plane component of the magnetization perturbation is much larger than that to the out-of-plane component both around and below resonance. The reason for this is that, when the magnetization is in-plane, the only contributions to the effective magnetic field are the applied bias and crystal anisotropy. When it is out-of-plane however, the demagnetization will also contribute, leading to a larger total effective

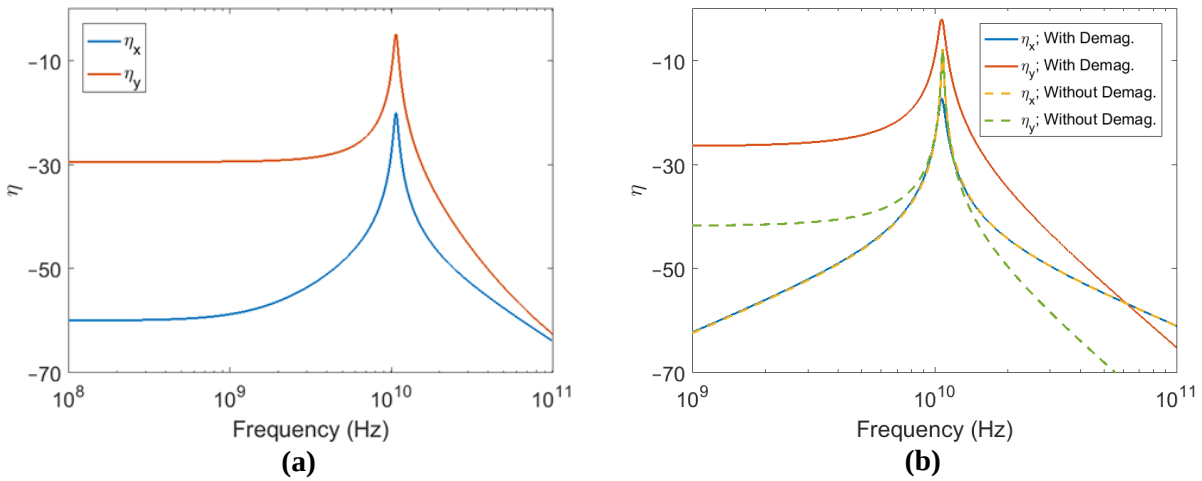

Figure 17. (a) Demagnetized case. (b) Comparison between cases with and without demagnetization.

magnetic field. By (3), this entails that magnetization perturbation will be larger out-of-plane as opposed to in-plane for a material with a given amount of energy sustained through applied stress. From the symbolic expressions, the fact that demagnetization contributes to a larger effective magnetic field only when the magnetization is out of plane is exhibited in (54), which shows the effective magnetic field dependent constant B_1 to have an additional term as compared with B_2. The larger B_1 then leads to a larger in-plane coupling coefficient in accordance with (51).

Comparing with the 100 Oe plot of Figure 16 (a), which corresponds to the same scenario but with negligible demagnetization, it is also seen that demagnetization acts to increase the resonance frequency. This is because of the field dependence of the resonance frequency (51) and, again, the fact that the demagnetization contribution will lead to a larger total effective magnetic field. These two effects of demagnetization on coupling for a thin film material with in-plane biasing are analogous to the increased in-plane permeability and increased ferromagnetic resonance frequency exhibited in the same types of materials as described by Kittel's equation [52].

In Figure 16 (a), it was shown that a stronger bias field raises the resonance frequency while reducing the amount of magnetoelastic coupling both at and below resonance. This reduction can be mitigated by employing demagnetization. Considering again a material with a thin film geometry biased in-plane, it is known that demagnetization contributes to increasing the total effective magnetic field. By (51) and (54), the bias field required to achieve a given resonance frequency will thus be weaker than that required for a material with negligible demagnetization. Given that, as discussed earlier, the demagnetization will only contribute to the effective magnetic field when the magnetization is out-of-plane, the effective magnetic field when the magnetization is in-plane involves only the weaker bias field and the crystal anisotropy. The result, by (3), is a larger magnetization perturbation as compared to that of the material with negligible demagnetization supposing a given amount of energy sustained through applied stress. In Figure 17 (b), the magnitudes of both η_x and η_y are plotted for the thin film magnetic material previously considered but now with optimal stress applied at an angle ϕ of 90° in the xy-plane. Also plotted are the magnitudes of η_x and η_y for the same material but with negligible demagnetization and a bias field of 3300 Oe to achieve the same resonance frequency as that of the thin film material. From the results, the thin film material is shown to exhibit higher amounts of coupling to the y-

component of magnetization perturbation at all frequencies as compared to the material with negligible demagnetization. Coupling to the x-component of magnetization perturbation is the same amongst the two materials except at resonance, where the material with negligible demagnetization has higher amounts of coupling.

4.5.2 Cubic crystal <111>

In section 4.3.2, it was found that the optimal direction of applied stress for a magnetic material with a cubic crystalline structure and <111> easy directions in general depends on both θ and ϕ. Investigating this matter further, the normalized magnitude of the transverse component of effective magnetic field contributed by the applied stress is computed using (48) and plotted as a function of θ in Figure 18 for several values of ϕ.

The magnetic materials considered were nickel Ni and magnetite Fe_3O_4, both having cubic crystalline structures and <111> easy directions. Some relevant characteristics of these materials are provided in Appendix H. The results for nickel are plotted in Figure 18 (a), and the results for

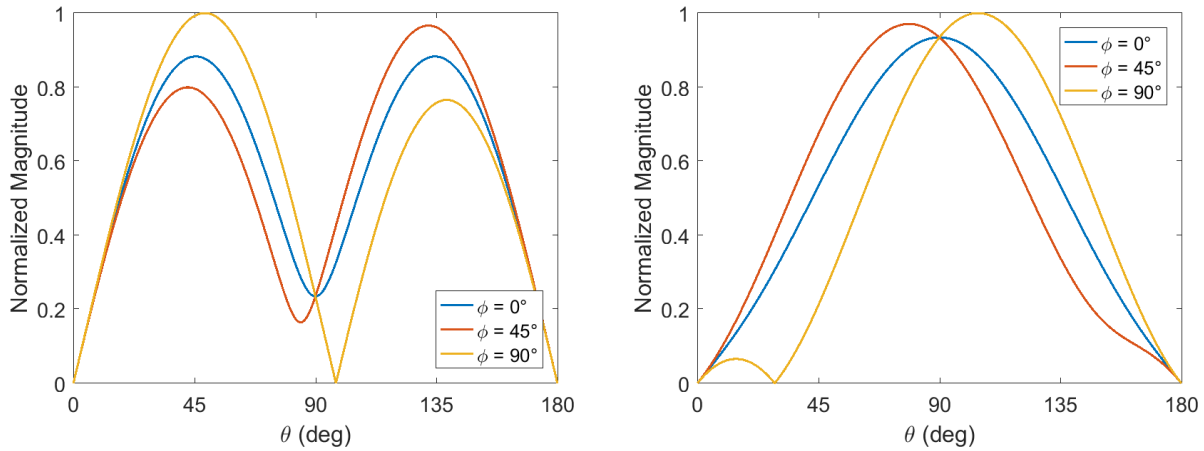

Figure 18. Normalized magnitude of the transverse component of effective magnetic field from applied stress for (a) nickel and (b) magnetite.

magnetite are plotted in Figure 18 (b). It is seen that the optimal θ for a given ϕ is approximately 45°, 90°, or 135° depending on the material. It is also seen that the choice of ϕ influences the

maximum possible magnitude of (48) that can be obtained. For both magnetite and nickel, a ϕ of 90° yields the largest possible magnitude in comparison to the other values of ϕ considered.

4.5.3 Other materials

The numerical evaluations for cubic crystals with <100> easy directions considered only iron. Other magnetic materials in this category will have different saturation magnetizations, crystal anisotropy constants, and magnetostriction constants. Based on the results of section 4.4 however, these differences will merely scale the amount of coupling or change the effective biasing field. All the core behaviors and effects exhibited through numerical evaluations using iron will remain valid. Analogously, the core results obtained from the numerical evaluations involving nickel and magnetite will remain valid for other cubic crystals with <111> easy directions. For hexagonal crystals with easy direction along the c-axis, again the amount of coupling may be scaled, or the effective biasing field may be changed, but the core behaviors and effects exhibited with iron will remain valid.

The numerical evaluations additionally considered only the demagnetization scenario of a thin film with in-plane biasing. With the other simple geometries, and for other $\hat{\boldsymbol{d}}$ directions, the effective biasing field may change along with the specific nature of the magnetoelastic coupling anisotropy with respect to angle of stress application, but the core insights regarding the effects of demagnetization remain valid.

4.5.4 Implications

The results of the numerical evaluation of the magnetoelastic coupling coefficient expressions (51) have several implications for the design and operation of mechanically driven magnetoelectric antennas. In order to achieve the best possible magnetoelastic coupling, and hence antenna performance, operation at the resonance frequency would be most appropriate. In this

regard, magnetic materials with lower damping will provide higher amounts of coupling at resonance. The primary means of tuning the resonance frequency to match a desired operating frequency is through the applied bias field strength. Unfortunately, it is an unavoidable fact that higher resonance frequencies are associated with reduced amounts of coupling, thus lower operating frequencies are recommended where possible. This reduction can be mitigated however through the choice of material geometry. For example, thin film materials biased in-plane were shown to mitigate the reductions in coupling to the in-plane component of magnetization.

The results of the numerical evaluation of the transverse effective magnetic field component (48) indicate that special care must be taken with regards to applied stress for cubic crystals with <111> easy directions. The optimal direction of applied stress for these crystals is dependent on material constants and is described not only by angle of application with respect to the dominant magnetization term θ, but also angle of application in the plane transverse to the dominant magnetization term ϕ.

CHAPTER 5

CONCLUSION

5.1 Summary

The potential radio frequency applications of spin dynamics extends far beyond their use solely for the design of nonreciprocal or tunable devices. In the first part of this dissertation, spin dynamics were assessed in the context of a new type of sensor called the RPM sensor. By using the nonlinearities inherent to spin dynamics for parametric amplification, this sensor is able to exhibit simultaneously a high sensitivity, small size, and low power consumption. The RPM sensor was theoretically characterized, and the theory was validated through micromagnetic simulations. A prototype RPM sensor was constructed and experimentally characterized. It was shown not only that the experimental characteristics agree very well with the theoretical predictions, but also that the 11.6 $pT/Hz^{1/2}$ sensitivity achieved with a power consumption of -41 dBm and a sensor volume of 0.0564 mm^3 is already competitive with existing sensors.

In the second part of this dissertation, spin dynamics were assessed in the context of a new type of antenna called the mechanically driven magnetoelectric antenna. To address a major deficiency in the approaches to modeling the antenna, the magnetoelastic coupling between spin dynamics and mechanical strain was analyzed in detail. This coupling is not only necessary for antenna operation, but it plays a crucial role in overall antenna performance. From the physics governing magnetoelastic coupling, conditions were derived to maximize it. These conditions were seen to be consistent with findings from experimental studies in literature. Explicit relations between the coupling and parameters of antenna operation and material properties were also derived and numerically evaluated. The results provide insight into the nature of magnetoelastic

coupling and the factors that influence it as well as guidance for antenna design and operation choices.

5.2 Outlook

Given that RPM sensors are a brand-new technology, the competitive performance already exhibited by the prototype as compared to existing sensors is very promising. This is especially true given that, as discussed in section 3.3.5, the quality of the YIG film used was worse than the quality of YIG crystals widely available today, causing an easily remedied decline in the sensitivity. RPM sensors still have much room for improvement with further research. One avenue of improvement is of course through a more detailed survey of the magnetic material employed. Materials with lower linewidths at a given frequency of operation will yield superior sensitivities. Another avenue of improvement is through an investigation into methods of spin wave suppression. For the prototype sensor, spin wave generation when the pump power is large [28] increases loss in the system and inhibits energy coupling into the uniform spin precession mode upon which RPM operation is contingent. Means of spin wave suppression will allow for a larger pump power and thus higher attainable sensitivities. A potential approach in this regard could be through the appropriate choice of precession resonance frequency [53], where higher frequencies have been shown to be less susceptible to spin wave generation. For RPM sensors to ultimately be widely implemented, further research is also needed from a standpoint of holistic practical design.

While not quite as new a technology as RPM sensors, mechanically driven magnetoelastic antennas are still in the infancy of their development. Successful realizations have been few and far between, and this is due in part to the nature of their operation which makes them difficult to model and simulate. Spin dynamics and magnetoelastic coupling, while certainly being crucial components of the operation, are by no means the sole components. A complete description of

mechanically driven magnetoelastic antennas would also require a consideration of electrodynamics as governed by Maxwell's equations [6], elastodynamics as governed by acoustic field theory [54], and the coupling between all the dynamics using constitutive relations [51]. Both the high degree of coupling and the vastly different spatial scales of the dynamics involved contribute to the modeling and simulation difficulties. The complete description is ultimately necessary to rigorously account for processes such as system resonance, mechanical loss, or electromagnetic radiation and, so far, attempts at a complete description have only been made with numerical approaches [51]. Unfortunately, these approaches provide little intuition or guidance for design purposes and so future research would need to take an analytical approach. In this regard, the results of this dissertation serve as a good starting point.

APPENDIX

A. Circuit Model Component Expressions

General expressions for the values of the RPM sensor circuit model components of Figure 3 are provided in Table 6, where A_m is the cross-sectional area of the magnetic material orthogonal to the axis of the loop. In SI units, $\omega_m = \mu_0 \gamma M_s$ and $\omega_h = \mu_0 \gamma H_0$. As usual, ω_0 is the resonant frequency of precession.

Circuit Component	No Demagnetization	Thin Film Biased In-Plane
R_m	$\frac{L_0 A_m}{A}\frac{\omega_m}{2\alpha}$	$\frac{L_0 A_m}{A}\frac{\omega_m \omega_0^2}{\alpha\omega_h(2\omega_h+\omega_m)}$
L_m	$\frac{L_0 A_m}{A}\frac{\omega_m}{\omega_0}$	$\frac{L_0 A_m}{A}\frac{\omega_m}{\omega_h}$
C_m	$\frac{A}{L_0 A_m}\frac{1}{\omega_m \omega_0}$	$\frac{A}{L_0 A_m}\frac{\omega_h}{\omega_m \omega_0^2}$

Table 6. Circuit model component expressions.

B. Ferrite-Core Inductive Sensor Sensitivity

For a ferrite-core inductive sensor, sensitivity is defined as the rms magnetic signal flux density that induces an open circuit rms voltage V_i equal to the rms noise voltage in a unit of bandwidth V_n. The noise voltage is attributed to the thermal noise of the conductive loop and so

$$V_n = \sqrt{4kTR_0} \tag{55}$$

where R_0 is the resistance of the loop. By using (31), (33), and (55), sensitivity can be expressed as

$$\delta B_{s,i} = \frac{\sqrt{4kTR_0}}{\mu_r N A \omega_s}. \tag{56}$$

where μ_r is the relative permeability of the ferrite core. Using $L_i = \mu_r \mu_0 N^2 A/l$ and $Q_i = \omega_s L_i / R_0$ for the loop inductance and quality factor respectively, where l is the axial length of the loop, (56) becomes

$$\delta B_{s,i} = \sqrt{\frac{4\mu_0 kT}{\mu_r v \omega_s Q_i}}$$

where v is the volume of the loop.

C. Pump Power Measurement

The pump power is determined using the results of a VNA measurement where the inductive sensor with YIG film, pump loop, and permanent magnets are configured as in Figure 9. Port 1 of the VNA was connected to the inductive sensor, and port 2 was connected to the pump loop. With the input power of the VNA set to -40 dBm, the results of an S12 measurement are shown in Figure 19. The peak S21 value, which occurs at the resonance frequency of the magnetic material, is -25.00 dB. Using this result as well as the fact that the prototype RPM sensor is matched to 50 Ω at the resonance frequency, when the pump loop is driven with a 50 Ω source and

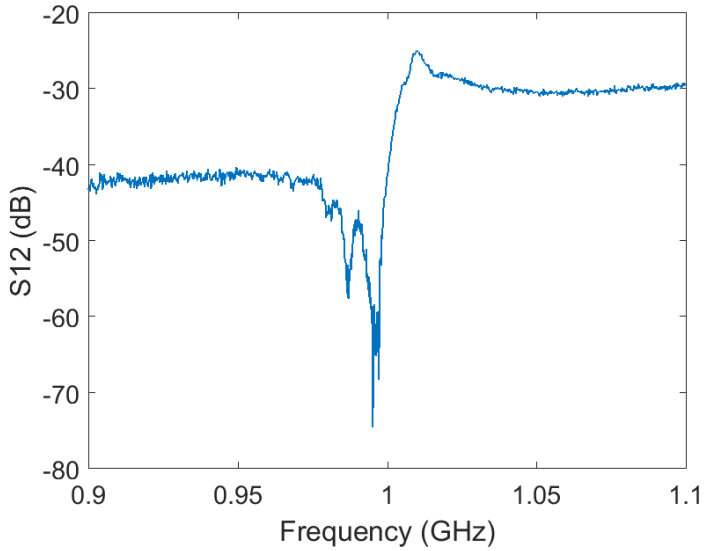

Figure 19. S12 measurement to determine pump power.

the inductive sensor is loaded with 50 Ω the pump power can be found to be -25.00 dB with respect to the available power from the source.

D. Signal Coil Circuit Model

The circuit model for the signal coil was found through curve fitting to measurements made with a current probe [55]. The model is shown in Figure 20 (a). For 1 V applied to the coil at various frequencies by a 50 Ω source, a plot of both the current found from the model and that measured with the current probe is provided in Figure 20 (b).

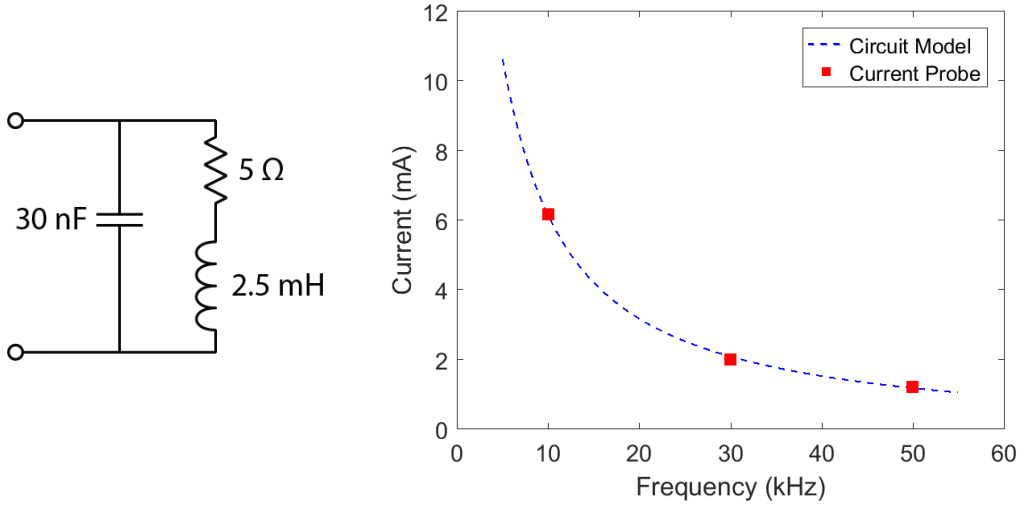

Figure 20. (a) Signal coil circuit model. (b) Comparison of current found from the model and that measured with the probe.

E. Biot-Savart Application to Signal Coil

The magnetic signal field is computed from the signal coil current I using the Biot-Savart law (1). The coil is modeled as an N turn rectangular current path with sides of length a and b where the observation point is located a distance d along the center axis of the rectangle. This model is shown in Figure 21 (a). An analytical expression for the field can be derived by considering the contributions from each side of the rectangle.

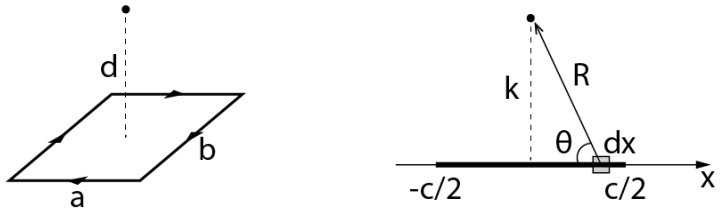

(a) **(b)**

Figure 21. (a) Coil model. (b) Field contribution from a straight, finite-length path.

The field contribution from a side of the rectangular current path is found by evaluating the Biot-Savart law for a straight, finite-length path with current NI, where the observation point is located on the perpendicular bisector of the path. This scenario is depicted in Figure 21 (b) for a path of length c, where the distance from the path to the observation point is k. The magnitude of the field contribution as a function of c and k can be written from (1) to be

$$H(c,k) = \frac{NI}{4\pi}\left|\int_{c/2}^{-c/2} \frac{\sin(\theta)\,dx}{R^2}\right| = \frac{NI}{2\pi}\left|\int_{c/2}^{0} \frac{\sin(\theta)\,dx}{R^2}\right|.$$

where, since $R = \sqrt{x^2 + k^2}$ and $\sin(\theta) = k/R$, the integrand is an even function of x. The variable of integration can be changed to θ by using the relations $R = k/\sin(\theta)$ and $x = k/\tan(\theta)$ to solve

$$H(c,k) = \frac{NI}{2\pi}\left|\int_{\theta_0}^{\pi/2} \frac{\sin(\theta)\,d\theta}{k}\right| = \frac{NI}{2\pi k}\cos(\theta_0) = \frac{NI}{2\pi k}\frac{c}{\sqrt{c^2 + 4k^2}}.$$

The total field is the sum of the contributions from each side of the rectangular current path. From Figure 21 (a), it is clear that the contributions from opposite sides will cancel to leave only an axial component. The total field then has a magnitude

$$H_{total} = \frac{2b}{\sqrt{b^2 + 4d^2}} H\left(a, \sqrt{\frac{b^2}{4} + d^2}\right) + \frac{2a}{\sqrt{a^2 + 4d^2}} H\left(b, \sqrt{\frac{a^2}{4} + d^2}\right).$$

(57)

F. SCR Theory Computation Values

Variable	Value	
H_0	70 Oe	
M_s	140 kA/m	
Q	135.95	
I	6.15 mA	(V = 1 V; f = 10 kHz)
	2.09 mA	(V = 1 V; f = 30 kHz)
	1.18 mA	(V = 1 V; f = 50 kHz)
	12.30 mA	(V = 2 V; f = 10 kHz)
	4.18 mA	(V = 2 V; f = 30 kHz)
	2.36 mA	(V = 2 V; f = 50 kHz)
H_s	355.3 mA/m	(V = 1 V; f = 10 kHz)
	120.6 mA/m	(V = 1 V; f = 30 kHz)
	68.1 mA/m	(V = 1 V; f = 50 kHz)
	710.6 mA/m	(V = 2 V; f = 10 kHz)
	241.2 mA/m	(V = 2 V; f = 30 kHz)
	136.2 mA/m	(V = 2 V; f = 50 kHz)

Table 7. Values for the computation of the theoretical SCR.

G. Sensitivity Computation Values

Values related to the computation of measured sensitivity are provided in Table 8 and those related to the computation of theoretical sensitivity are provided in Table 9. The damping noise V_n was found assuming the resistance R_m to be 50 Ω.

Variable	Value	
V_n	0.895 nV/Hz$^{1/2}$	
$V_{n,LNA}$	1.428 nV/Hz$^{1/2}$	
Q_u	271.90	
Q_L	135.95	
D_n	0.265	
I	61.5 uA	(f = 10 kHz)
	42.1 uA	(f = 15 kHz)
	20.9 uA	(f = 30 kHz)

H_s	6.80 mA/m	(f = 10 kHz)
	4.66 mA/m	(f = 15 kHz)
	2.31 mA/m	(f = 30 kHz)
SNR	41.51 dB	(f = 10 kHz)
	38.20 dB	(f = 15 kHz)
	33.43 dB	(f = 30 kHz)

Table 8. Values for the computation of the measured sensitivity.

Variable	Value
H_0	70 Oe
M_s	140 kA/m
Q_u	271.9
P_0	-41.0 dBm
T	290 K

Table 9. Values for the computation of the theoretical sensitivity.

H. Magnetic Material Properties

Several magnetic materials and their associated properties are provided in Table 10 [5] [56] [57].

Material	M_s (emu/cm^3)	K_1 (erg/cm^3)	λ (10^{-6})
Fe	1714	4.8e5	λ_{100} = 21 λ_{111} = -21
Ni	484	-5e4	λ_{100} = -46 λ_{111} = -24
Fe_3O_4	480	-1.1e5	λ_{100} = -20 λ_{111} = 78
Co	1297	2e6	λ_A = -45 λ_B = -95 λ_C = 110

Table 10. Magnetic material properties.

REFERENCES

[1] A. J. B. Fuller, Ferrites at Microwave Frequencies, London: Peter Peregrinus, 1987.

[2] W. Gu, K. Luong, Z. Yao, H. Cui and Y. E. Wang, "Ferromagnetic Resonance-Enhanced Electrically Small Antennas," *IEEE Transactions on Antennas and Propagation,* vol. 69, no. 12, pp. 8304-8314, 2021.

[3] D. Grundler, "Reconfigurable magnonics heats up," *Nature Physics,* vol. 11, no. 6, pp. 438-441, 2015.

[4] M. M. Vopson, "Fundamentals of Multiferroic Materials and Their Possible Applications," *Critical Reviews in Solid State and Materials Sciences,* vol. 40, no. 4, pp. 223-250, 2015.

[5] B. D. Cullity and C. D. Graham, Introduction to Magnetic Materials, Hoboken, New Jersey: John Wiley & Sons, 2011.

[6] D. J. Griffiths, Introduction to Electrodynamics, Upper Saddle River, New Jersey: Prentice Hall, 1999.

[7] D. D. Stancil and A. Prabhakar, Spin Waves, New York, New York: Springer, 2009.

[8] B. Lax and K. J. Button, Microwave Ferrites and Ferrimagnetics, McGraw-Hill Book Company, 1962.

[9] V. G. Harris, "Modern Microwave Ferrites," *IEEE Transactions on Magnetics,* vol. 48, no. 3, pp. 1075-1104, 2012.

[10] MTI Corporation, "YIG Epi. Film on GGG," MTI Corporation, [Online]. Available: https://www.mtixtl.com/yigepitacialfilmonggg.aspx. [Accessed 6 April 2022].

[11] N. A. Spaldin, "Multiferroics beyond electric-field control of magnetism," *Proceedings of the Royal Society A,* vol. 476, no. 2233, 2020.

[12] A. Grosz, M. J. Haji-Sheikh and S. C. Mukhopadhyay, Eds., High Sensitivity Magnetometers, Springer, 2017.

[13] B. E. A. Saleh and M. C. Teich, Fundamentals of Photonics, Hoboken, New Jersey: John Wiley & Sons, 2007.

[14] J. Clarke and A. I. Braginski, Eds., The SQUID Handbook, Wiley-VCH, 2004.

[15] J. Lenz and S. Edelstein, "Magnetic sensors and their applications," *IEEE Sensors Journal,* vol. 6, no. 3, pp. 631-649, 2006.

[16] C. Deans, L. Marmugi and F. Renzoni, "Sub-picotesla widely tunable atomic magnetometer operating at room-temperature in unshielded environments," *Review of Scientific Instruments,* vol. 89, no. 8, 2018.

[17] S. Tumanski, "Induction coil sensors - a review," *Measurement Science and Technology,* vol. 18, no. 3, pp. R31-R46, 2007.

[18] S. K. Harriman, E. W. Paschal and U. S. Inan, "Magnetic Sensor Design for Femtotesla Low-Frequency Signals," *IEEE Transactions on Geoscience and Remote Sensing,* vol. 48, no. 1, pp. 396-402, 2010.

[19] R. C. Chaves, P. P. Freitas, B. Ocker and W. Maass, "Low frequency picotesla field detection using hybrid MgO based tunnel sensors," *Applied Physics Letters,* vol. 91, no. 10, 2007.

[20] F. Primdahl, "The fluxgate magnetometer," *Journal of Physics E: Scientific Instruments,* vol. 12, no. 4, pp. 241-253, 1979.

[21] M. Inoue and et al., "Investigating the use of magnonic crystals as extremely sensitive magnetic field sensors at room temperature," *Applied Physics Letters,* vol. 98, no. 13, 2011.

[22] T. Koda, S. Muroga and Y. Endo, "Highly Sensitive Magnetic Field Sensing Using Magnetization Dynamics in Yttrium Iron Garnet Single-Crystal Thin Films," *IEEE Transactions on Magnetics,* vol. 55, no. 7, pp. 1-4, 2019.

[23] B. Yan, W. Zhu, L. Liu, K. Liu and G. Fang, "Design of Induction Magnetometer Receiving Sensor for Through-the-Earth Communications," *IEEE Sensors Journal,* vol. 15, no. 2, pp. 1139-1144, 2015.

[24] G. B. Hospodarsky, "Spaced-based search coil magnetometers," *Journal of Geophysical Research: Space Physics,* vol. 121, no. 12, pp. 12,068-12,079, 2016.

[25] M. Sarracanie, C. D. LaPierre, N. Salameh, D. E. J. Waddington, T. Witzel and M. S. Rosen, "Low-Cost High-Performance MRI," *Scientific Reports,* vol. 5, no. 1, 2015.

[26] D. M. Pozar, Microwave Engineering, 4th ed., Hoboken: John Wiley & Sons, 2012.

[27] H. Cui, Z. Yao and Y. E. Wang, "Coupling Electromagnetic Waves to Spin Waves: A Physics-Based Nonlinear Circuit Model for Frequency-Selective Limiters," *IEEE Transactions on Microwave Theory and Techniques,* vol. 67, no. 8, pp. 3221-3229, 2019.

[28] H. Suhl, "The Nonlinear Behavior of Ferrites at High Microwave Signal Levels," *Proceedings of the IRE,* vol. 44, no. 10, pp. 1270-1284, 1956.

[29] W. L. Stutzman and G. A. Thiele, Antenna Theory and Design, Hoboken, New Jersey: John Wiley & Sons, 2013.

[30] J. B. Goodenough, "Summary of losses in magnetic materials," *IEEE Transactions on Magnetics,* vol. 38, no. 5, pp. 3398-3408, 2002.

[31] P. M. Gradzki and F. C. Lee, "Domain wall resonance and its effect on losses in ferrites," in *PESC '91 Record 22nd Annual IEEE Power Electronics Specialists Conference*, Cambridge, 1991.

[32] E. C. Snelling, Soft Ferrites, London: Iliffe Books, 1969.

[33] W. F. Brown Jr., Micromagnetics, Interscience, 1963.

[34] M. J. Donahue and D. G. Porter, "OOMMF User's Guide, Version 1.0," National Institute of Standards and Technology, Gaithersburg, 1999.

[35] J. Leliaert and J. Mulkers, "Tomorrow's micromagnetic simulations," *Journal of Applied Physics*, vol. 125, no. 18, 2019.

[36] K&J Magnetics, Inc., "BZ0Z04-N52," K&J Magnetics, Inc., [Online]. Available: https://www.kjmagnetics.com/proddetail.asp?prod=BZ0Z04-N52. [Accessed 7 April 2022].

[37] Rogers Corporation, "RO4000 Series High Frequency Circuit Materials," Rogers Corporation, [Online]. Available: https://rogerscorp.com/-/media/project/rogerscorp/documents/advanced-electronics-solutions/english/data-sheets/ro4000-laminates-ro4003c-and-ro4350b---data-sheet.pdf. [Accessed 8 April 2022].

[38] Analog Devices, "EVAL-ADL5390," Analog Devices, [Online]. Available: https://www.analog.com/en/design-center/evaluation-hardware-and-software/evaluation-boards-kits/eval-adl5380.html. [Accessed 10 April 2022].

[39] RF-Lambda, "Wide Band RF Benchtop AC Amplifier," RF-Lambda, [Online]. Available: https://www.rflambda.eu/pdf/acamplifier/RAMP00M45GA.pdf. [Accessed 9 April 2022].

[40] M. C. Budge and M. P. Burt, "Range correlation effects in radars," in *The Record of the 1993 IEEE National Radar Conference*, Lynnfield, 1993.

[41] R. J. Prance, T. D. Clark and H. Prance, "Compact room-temperature induction magnetometer with superconducting quantum interference device level field sensitivity," *Review of Scientific Instruments*, vol. 74, no. 8, pp. 3735-3739, 2003.

[42] J. Lei, C. Lei and Y. Zhou, "Micro Fluxgate Sensor using Solenoid Coils Fabricated by MEMS Technology," *Measurement Science Review*, vol. 12, no. 6, pp. 286-289, 2012.

[43] T. Nan and et al., "Acoustically actuated ultra-compact NEMS magnetoelectric antennas," *Nature Communications*, vol. 8, no. 1, 2017.

[44] Z. Yao, Y. E. Wang, S. Keller and G. P. Carman, "Bulk Acoustic Wave-Mediated Multiferroic Antennas: Architecture and Performance Bound," *IEEE Transactions on Antennas and Propagation*, vol. 63, no. 8, pp. 3335-3344, 2015.

[45] C. Dong and et al., "A Portable Very Low Frequency (VLF) Communication System Based on Acoustically Actuated Magnetoelectric Antennas," *IEEE Antennas and Wireless Propagation Letters*, vol. 19, no. 3, pp. 398-402, 2020.

[46] G. Xu, S. Xiao, Y. Li and B.-Z. Wang, "Modeling of electromagnetic radiation-induced from a magnetostrictive/piezoelectric laminated composite," *Physics Letters A*, vol. 385, 2021.

[47] R. L. Kubena, X. Pang, K. G. Lee, Y. K. Yong and W. S. Wall, "Wide-band multiferroic quartz MEMS antennae," *Journal of Physics: Conference Series*, vol. 1407, no. 1, 2019.

[48] F. Rangriz, A. Khaleghi and I. Balasingham, "Wireless Link for Micro-scale Biomedical Implants using Magnetoelectric Antennas," in *2020 14th European Conference on Antennas and Propagation (EuCAP)*, 2020.

[49] D. Labanowski, A. Jung and S. Salahuddin, "Power absorption in acoustically driven ferromagnetic resonance," *Applied Physics Letters*, vol. 108, no. 2, 2016.

[50] H. Zhou, A. Talbi, N. Tiercelin and O. Bou Matar, "Multilayer magnetostrictive structure based surface acoustic wave devices," *Applied Physics Letters,* vol. 104, no. 11, 2014.

[51] Z. Yao and et al., "Modeling of Multiple Dynamics in the Radiation of Bulk Acoustic Wave Antennas," *IEEE Journal on Multiscale and Multiphysics Computational Techniques,* vol. 5, pp. 5-18, 2020.

[52] Q. Xu, W. Gu and Y. E. Wang, "Two dimensional (2D) complex permeability characterization of thin film ferromagnetic material," in *2016 IEEE Conference on Antenna Measurements & Applications (CAMA)*, Syracuse, 2016.

[53] T. Qu and et al., "Nonlinear Magnon Scattering Mechanism for Microwave Pumping in Magnetic Films," *IEEE Access,* vol. 8, pp. 216960-216968, 2020.

[54] B. A. Auld, Acoustic Fields and Waves in Solids, vol. I, John Wiley & Sons, 1973.

[55] YPioneer, "A622 Current Probe," Yangzhong Pioneer, [Online]. Available: http://www.ypioneer.com/ypioneer_Product_2008148823.html. [Accessed 10 April 2022].

[56] J. M. D. Coey, Magnetism and Magnetic Materials, New York, New York: Cambridge University Press, 2009.

[57] G. Consolo, S. Federico and G. Valenti, "Magnetostriction in transversely isotropic hexagonal crystals," *Phys. Rev. B,* vol. 101, no. 1, 2020.